Chemical Geology 649 (2024) 121978

Contents lists available at ScienceDirect

Chemical Geology

journal homepage: www.elsevier.com/locate/chemgeo

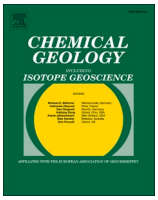

Research Paper

Olivine formation processes and fluid pathways in subducted serpentinites revealed by in-situ oxygen isotope analysis (Zermatt-Saas, Switzerland)

Michelle Ulrich [a,*], Daniela Rubatto [a,b], Jörg Hermann [a], Thorsten A. Markmann [a], Anne-Sophie Bouvier [b], Etienne Deloule [c]

[a] Institute of Geological Sciences, University of Bern, Bern CH-3012, Switzerland
[b] Institute des Sciences de la Terre, University of Lausanne, Lausanne CH-1015, Switzerland
[c] Université de Lorraine, CNRS, CRPG, 54500 Vandœuvre-lès-Nancy, France

ARTICLE INFO

Editor: S Aulbach

Keywords:
Serpentinite dehydration
Olivine formation
Oxygen isotopes
Isotopic equilibrium

ABSTRACT

Dehydration of serpentinites plays a crucial role in mass transfer into the Earth's interior by releasing aqueous fluids and forming new minerals. These minerals, such as metamorphic olivine, can serve as tracers of fluid-related processes. High-pressure (HP) antigorite, metamorphic olivine, and coexisting magnetite in serpentinites from a continuous, km-scale outcrop within the Zermatt-Saas HP ophiolite were analyzed in situ for trace elements and oxygen isotopes to identify differences in the initial serpentinization conditions and to investigate fluid pathways during subduction-related metamorphism. The oxygen isotopic composition, and As and Sb concentrations in antigorite reveal two distinct serpentinization conditions within the studied region: i) high As and Sb (1–25 μg/g and 0.5–5 μg/g, respectively), coupled with $\delta^{18}O$ of +6 to +7 ‰, suggesting serpentinization at relatively low temperatures near the seafloor, and ii) low As and Sb (0.03–5 μg/g and ≤ 0.1 μg/g, respectively), coupled with mostly lower $\delta^{18}O$ of +4 to +6 ‰, suggesting serpentinization at higher temperatures by interaction with fluids deeper below the seafloor.

Olivine produced in situ by the brucite + antigorite dehydration reaction during subduction shows isotopic equilibrium with antigorite, and coexisting magnetite with $\Delta^{18}O_{Atg\text{-}Ol}$ of +1.5–2.5 ‰ and $\Delta^{18}O_{Ol\text{-}Mt}$ of ~+3 ‰ at reaction temperature conditions of 550–600 °C. The obtained isotopic signatures of metamorphic olivine with $\delta^{18}O$ values of +1 to +2 ‰ and + 4 to +5 ‰ correspond to two different isotopic compositions of the released fluid of +5 to +6 ‰ and + 8 to +9 ‰ at these temperature conditions. This suggests that fluids released from subducted serpentinites may have variable $\delta^{18}O$ under forearc conditions. The presence of fluids with variable $\delta^{18}O$ can cause olivine in structures associated with fluid flow (e.g., shear bands, shear zones and veins) to be in isotopic equilibrium with magnetite, but in either isotopic equilibrium or disequilibrium with antigorite. Isotopic equilibrium with antigorite is achieved when the fluid responsible for olivine crystallization is internally derived. Isotopic disequilibrium is due to an externally derived fluid released by dehydration of serpentinite with a different isotopic composition than the serpentinite with which the fluid interacts. The restricted occurrence of non-equilibrated olivine only in shear bands and nearly pure Ol-veins indicates channelized fluid flow in subduction zone settings and demonstrates that isotopic disequilibrium can be used as a tracer for fluid infiltration.

1. Introduction

Serpentinites play an important role in elemental and fluid cycling in subduction zones, where the highest mass fluxes between Earth's crust and mantle occur (e.g., Ulmer and Trommsdorff, 1995; Scambelluri et al., 1995, 2004b, 2019; Rüpke et al., 2004; Deschamps et al., 2013). Fully serpentinized oceanic mantle can store up to 13 wt% water, which is released as aqueous fluid into the mantle wedge in a series of dehydration reactions due to the breakdown of the hydrous minerals during prograde subduction (Ulmer and Trommsdorff, 1995; Rüpke et al., 2004). In the first dehydration reaction, brucite + antigorite produces metamorphic olivine, chlorite, and aqueous fluid (Ulmer and Trommsdorff, 1995; Scambelluri et al., 2004a; Kempf et al., 2020), releasing between 3.4 and 7.2 wt% fluid (Kempf et al., 2020). With prograde

* Corresponding author.
E-mail address: michelle.ulrich@unibe.ch (M. Ulrich).

https://doi.org/10.1016/j.chemgeo.2024.121978
Received 13 November 2023; Received in revised form 1 February 2024; Accepted 2 February 2024
Available online 3 February 2024

subduction and higher temperatures, antigorite decomposes into metamorphic olivine, orthopyroxene, chlorite, and aqueous fluid (e.g., Trommsdorff et al., 1998; Padrón-Navarta et al., 2011). Complete dehydration is eventually reached when chlorite + orthopyroxene react to form metamorphic olivine, garnet, and aqueous fluid (Evans and Trommsdorff, 1978; Trommsdorff et al., 2000; Lakey and Hermann, 2022). Aqueous fluids released from serpentinites carry volatiles and fluid-mobile elements such as S, Cl, B and As (e.g., Bebout, 1995; Deschamps et al., 2013; Scambelluri et al., 2019) and influence important geodynamic processes such as arc magmatism (e.g., Schmidt and Poli, 1998), mantle wedge metamorphism (Rubatto and Angiboust, 2015; Bovay et al., 2021; Spandler et al., 2011), and earthquakes (Hacker et al., 2003; Bloch et al., 2018).

The fluids produced ultimately escape either via channelized fracture-like pathways (e.g., Padrón-Navarta et al., 2010; Herms et al., 2012; Ague, 2014) or via pervasive porosity waves (Ague, 2014; Connolly and Podladchikov, 2007; Miller et al., 2003; Skarbek and Rempel, 2016), with metamorphic olivine being an indicator of the production and transport of the fluid. In-situ olivine formation in serpentinites is controlled by the distribution of former brucite (Kempf et al., 2020). In the case of a closed system, (oxygen) isotope equilibrium fractionation is expected between the minerals of the assemblage that are stable under given P-T conditions. Recently, it has been proposed that olivine can also form in fluid channels in serpentinite (Huber et al., 2022), where a reactive fluid with a low Si potential triggers antigorite destabilization with concomitant olivine precipitation. This model is particularly interesting for explaining olivine in fluid path structures such as shear bands and veins, where the modal abundance of olivine exceeds the amount of olivine produced by the dehydration reaction of antigorite with brucite (Kempf et al., 2020; Peters et al., 2020). Thus, olivine in shear bands and veins requires reactive fluids, which can be either locally or externally sourced, potentially leading to an isotopic disequilibrium between olivine and antigorite (Plümper et al., 2017).

Bulk oxygen isotope studies have shown that subducted serpentinites can have different isotopic signatures within the same ophiolitic unit with a variability of up to 5 ‰ (Cartwright and Barnicoat, 1999; Früh-Green et al., 2001; Alt et al., 2012; Gregory and Taylor, 1981). These studies attributed the large variation in $\delta^{18}O$ of subducted serpentinites to oceanic hydration at variable temperatures. In fact, it has long been recognized that differences in temperature, fluid isotope composition and fluid/rock ratio during oceanic alteration of the mantle rocks result in significant shifts away from the mantle oxygen isotopic composition ($\delta^{18}O \sim +5.5 \pm 0.2$ ‰; Mattey et al., 1994). Oceanic alteration can produce either high $\delta^{18}O$ values up to +13 ‰ by low temperature serpentinization near the ocean surface or $\delta^{18}O$ values as low as ~ +3 ‰ during high temperature serpentinization (e.g., Gregory and Taylor, 1981; Wenner and Taylor, 1971; Früh-Green et al., 1996). Whereas earlier studies were carried out on bulk rocks or serpentine separates, more recent studies have used in-situ analysis by secondary ion mass spectrometry (SIMS) to investigate the different serpentinite microtextures, particularly in oceanic serpentinites (Rouméjon et al., 2018; Scicchitano et al., 2020; Scicchitano et al., 2022; Vesin et al., 2023). This opens the possibility to also address the isotopic signature of minerals associated with different fluid flow textures in subducted serpentinites, such as olivine in shear bands and veins, and to investigate whether the fluids involved were locally or externally sourced.

The scope of this study is to investigate the variability in the isotopic composition of antigorite and olivine in subducted serpentinite, and their isotopic equilibrium or disequilibrium. These data are used to distinguish in-situ olivine and fluid production during the antigorite+brucite reaction from fluid migration and olivine crystallization during reactive fluid flow. Serpentinites from the Zermatt-Saas ophiolite were collected from a continuous, km-scale outcrop between the Upper and Lower Theodul Glacier (UTG and LTG), where the brucite+antigorite dehydration reaction occurred at 2.2–2.5 GPa and ~ 550 °C (Kempf et al., 2020). The serpentinites in this area have varying meso- and microtextures. These textures range from rather undeformed and massive, to highly deformed, with a variable olivine content, and reflect different degrees and types of fluid flow. A microanalytical approach is used to assess the potential variability in the isotopic composition of antigorite and olivine. The approach combines in-situ oxygen isotope analysis by SIMS with major element measurements by electron microprobe analysis (EPMA) and trace element measurements by LA-ICP-MS, targeting different antigorite, olivine, and magnetite textures. The combined textural, elemental, and isotopic dataset allows to identify differences in the initial serpentinization setting (e.g., by As, Sb and B concentrations as demonstrated among others by Pettke and Bretscher, 2022) as well as isotopic (dis)equilibrium under the conditions of the antigorite+brucite dehydration reaction. Isotopic equilibrium or disequilibrium has implications for the olivine formation process as well as for the generation and migration of the released fluids and helps to distinguish between locally and externally sourced fluids.

2. Geological setting

The Zermatt-Saas ophiolite is a remnant of the Middle to Late Jurassic Piedmont-Ligurian oceanic lithosphere (e.g., Rubatto et al., 1998; Bearth, 1974) and is located in the South Penninic nappe stack in the Western Alps. This ophiolite marks the suture between the Adriatic continental crust and the European continental margin (e.g., Dal Piaz et al., 1999 and 2001; Escher and Beaumont, 1997) involved in the Alpine orogeny. The serpentinite body investigated in this study is located south of the village of Zermatt (Fig. 1).

The metaophiolite is composed of serpentinized ultramafic rocks, metabasites derived from both metagabbro and metabasalts, including lava flows and pillows, and associated metasediments that have undergone eclogite-facies conditions of 2.2–2.5 GPa and ~ 550–600 °C (Angiboust et al., 2009; Bearth, 1967; Bucher et al., 2005; Bucher and Grapes, 2009). Peak eclogite-facies conditions were reached during the subduction of the oceanic unit at 43–50 Ma (de Meyer et al., 2014; Lapen et al., 2003; Rubatto et al., 1998; Skora et al., 2015). Subsequently, the unit was rapidly exhumed within 2–5 Ma and overprinted by greenschist facies conditions at 400–500 °C and 0.4–0.6 GPa (Agard et al., 2009; Cartwright and Barnicoat, 2002).

The exhumed mantle in this locality underwent extensive Jurassic hydration forming serpentinites, followed by partial dehydration at HP during Eocene Alpine subduction. The petrology and chemistry of the serpentinites in this locality have been investigated in previous studies (e.g., Kempf et al., 2020; Li et al., 2004; Li et al., 2008; Seydoux and Baumgartner, 2013). Evidence for the hydration of the harzburgitic mantle is provided by widespread serpentinization associated with magnetite formation and rodingitization of mafic dykes (Li et al., 2004; Li et al., 2008; Kempf et al., 2020). Oceanic serpentinization is indicated by (i) $^{87}Sr/^{86}Sr$ of ~0.7071–0.7083 (Gilio et al., 2019; Bouilhol et al., 2022), which overlaps with the Jurassic seawater composition of $^{87}Sr/^{86}Sr = 0.7070$ (Peterman et al., 1970; Jones et al., 1994) and by (ii) the characteristic enrichment of fluid-mobile elements in serpentine such as B (10–30 μg/g), As (0.2–0.5 μg/g) and Sb (0.1–0.2 μg/g) (Gilio et al., 2019). Alpine subduction of the serpentinites under eclogite-facies conditions resulted in prograde metamorphism that recrystallized oceanic serpentine (mainly lizardite and chrysotile) to antigorite and formed metamorphic olivine (Kempf et al., 2020). Alpine subduction was also accompanied by major deformation events, resulting in foliated serpentinites and the development of shear zones (e.g., Li et al., 2004; Cartwright and Barnicoat, 2002; Seydoux and Baumgartner, 2013; Kempf et al., 2020). Exhumation of the serpentinites is indicated by late, crosscutting veins, e.g., tremolite-actinolite-talc-carbonate veins (Kempf et al., 2020). No mantle relic olivine or oceanic serpentine minerals are preserved. Minor lizardite and chrysotile, occurring mainly in veins, are products of secondary serpentinization during exhumation (e.g., Li et al., 2004; Kempf et al., 2020).

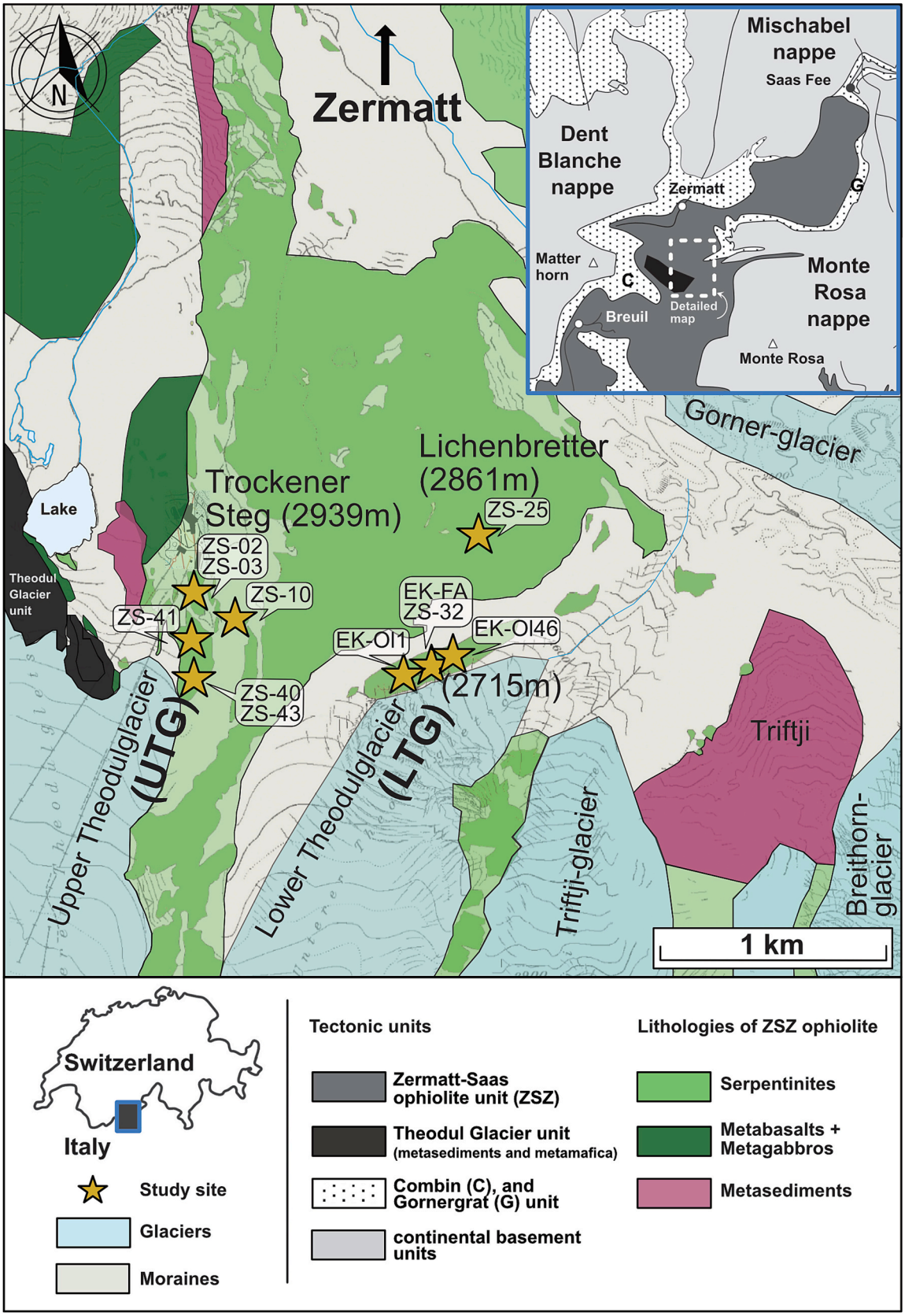

Fig. 1. Map of the Zermatt-Saas ophiolite in the area south of the village of Zermatt. The map is modified from Kempf et al. (2014) and is based on the original work of Bearth (1967) and further adapted according to Seydoux and Baumgartner (2013); Kempf et al. (2020) and Bucher et al. (2020). Samples collected south of Trockener Steg and Lichenbretter are labeled UTG, while samples collected further to the southeast from an outcrop near the Lower Theodulglacier are labeled LTG.

3. Sample description

Different types of serpentinite samples were collected from the outcrop between the UTG and LTG (Fig. 1 and Table 1), including Ol-free Atg-serpentinites, Atg-veins, Ol-bearing Atg-serpentinites, Ol-shear bands and shear zones, and Ol-veins (Fig. 2). Olivine in the Ol-Atg-serpentinite is patchy or mimics "zebra" stripes of Ol-rich and Ol-poor domains. The different types of serpentinites, which contain varying amounts of olivine between ~30–90 vol%, are exposed over the entire area between UTG and LTG. The outcrop part at LTG, which was previously described by Kempf et al. (2020), exposes the least deformed serpentinites compared to the outcrop part at UTG, which includes Trockener Steg and Lichenbretter. At LTG, portions of poorly foliated serpentinites (estimated at >15 vol%) are cut by straight Atg-veins, which in turn are cut by Ol-bands (Fig. 3E). In addition, meta-rodingite dykes and meta-Fe-Ti basalt dykes (now transformed to the assemblage vesuvianite, chlorite, grossular, diopside, epidote, clinozoisite, calcite and andradite, and to the assemblage Ti-clinohumite, Ti-chondrodite and andradite, respectively), cut each other at high angles (Li et al., 2008; Kempf et al., 2020; Li et al., 2004; Gilio et al., 2019). The undeformed portions of serpentinite are surrounded and cut by domains of higher deformation, which are present as a network of shear bands and localized shear zones. At UTG, serpentinites show strong foliation, and Ol-shear bands and shear zones are common. The larger, meter-wide shear zones can be traced for up to 100 m along strike. Rarely, some crosscutting veins and dykes and some undeformed serpentinites can be found, but they are minor and exposed in <5 vol% of the outcrop. Although the rocks are generally stronger deformed at UTG than at LTG, samples from both outcrop parts show variable deformation in different zones. Thin sections were cut perpendicular to the foliation whenever a foliation was visible.

3.1. Atg-serpentinite and Atg-veins

Samples ZS-02 and ZS-18 (Fig. 3) represent the Ol-free end member Atg-serpentinite. Sample ZS-18 is massive, and was collected at LTG (Fig. 3A), while sample ZS-02 from UTG shows a strong foliation (Fig. 3C). In the massive sample, antigorite forms randomly oriented crystals (~30 × 100 μm) and mm-sized patches consisting of fine-grained antigorite (~10 × 50 μm). Magnetite forms aggregates that

Table 1
Overview of investigated samples, their main assemblages and $\delta^{18}O$ values of mineral phases. The samples are arranged in order of increasing deformation / Ol texture.

Sample	Coordinates CH1903+/ LV95 Swiss coordinates	Description	Mineral assemblage	Structure / Ol texture	$\delta^{18}O$ (‰) antigorite	$\delta^{18}O$ (‰) olivine	$\delta^{18}O$ (‰) magnetite
ZS-18 (LTG)	2′622′875, 1′090′486	Massive Atg-serpentinite	Atg + Mt. ± Cb	Massive, not foliated Atg	6.74 ± 0.70, $n = 13$	No olivine	−0.79 ± 1.33, n = 9
ZS-19 (LTG)	2′622′877, 1′090′487	Atg-vein close to ZS-18	Atg + Mt	Massive, not foliated Atg	6.25 ± 0.60, $n = 36$	No olivine	n.a.
ZS-45 (LTG)	2′622′866, 1′090′485	Atg-vein between EK-FA and ZS-32	Atg + Mt	Massive, not foliated Atg	8.35 ± 1.55, $n = 20$	No olivine	−1.68 ± 2.17, $n = 5$
EK-FA (LTG)	2′622′866, 1′090′485	Massive Ol-Atg-serpentinite with relic mesh fabric	Ol + Atg + Mt. ± Chl ± Cb	Pervasively grown Ol1 + Ol2 bands	4.22 ± 0.70, $n = 11$	1.78 ± 0.84, $n = 20$	0.12 ± 1.99, $n = 7$
ZS-40 (UTG)	2′621′849, 1′090′467	Massive Ol-Atg-serpentinite with additional Ol-bands	Ol + Atg + Mt. ± Ti-Chu	Pervasively grown Ol1 + Ol2 bands	3.48 ± 0.90, $n = 12$	2.18 ± 0.77, $n = 9$	n.a.
ZS-43 (UTG)	2′622′005, 1′090′574	Ol-bands in Atg-serpentinite	Ol + Atg + Mt	Ol2 polygons	3.64 ± 0.38, $n = 13$	2.46 ± 0.31, $n = 15$	n.a.
ZS-10 (UTG)	2′622′018, 1′090′645	Ol-Atg-serpentinite with Ol-shear bands	Ol + Atg + Mt	Ol2 + few larger and patchy Ol-crystals (Ol1)	3.90 ± 0.52, n = 15	2.37 ± 0.50, $n = 10$	−0.86 ± 1.46, $n = 14$
ZS-25 (UTG)	2′622′645, 1′091′124	Foliated Ol-Atg-serpentinite with Ol-shear bands	Ol + Atg + Mt. ± relic Cr-spinel	Ol2 polygons in bands + few porphyroblasts	4.07 ± 0.57, $n = 32$	1.85 ± 0.65, $n = 27$	n.a.
ZS-41 (UTG)	2′622′005, 1′090′420	Ol-bands in Atg-serpentinite	Ol + Atg + Mt	Ol2 polygons	6.28 ± 0.84, $n = 17$	3.79 ± 0.87, n = 14	n.a.
ZS-32 (LTG)	2′622′878, 1′090′485	Ol-shear bands close to ZS-18	Ol + Atg + Mt. ± Cb ± Ti-Chu ± Ap	Ol2 polygons	6.55 ± 0.63, $n = 24$	1.57 ± 0.66, $n = 19$	−0.36 ± 2.04, $n = 16$
EK-Ol1 (LTG)	2′622′836, 1′090′457	Ol-rich shear zone	Ol + Atg + Mt. + Chl ± Cb ± Ti-Chu ± Ap	Ol2 polygons	6.14 ± 0.70, $n = 39$	1.39 ± 0.84, $n = 61$	−2.29 ± 1.14, n = 15
ZS-03 (UTG)	2′621′983, 1′090′578	Ol-rich shear zone with crosscutting Cb-vein	Ol + Atg + Mt. + Chl ± Cb ± relic Cr-spinel	Ol2 polygons + porphyroblasts	5.84 ± 0.70, $n = 18$	4.62 ± 0.46, n = 17	2.12 ± 1.86, n = 13
ZS-02 (UTG)	2′621′942, 1′090′627	Strongly foliated Atg-serpentinite	Atg + Mt	Foliated Atg	5.48 ± 0.60, n = 10	No olivine	1.41 ± 2.64, n = 17
EK-MF4 (LTG)	2′622′861, 1′090′394	Ol-veinlet crosscutting Ol-Atg-serpentinite	Ol + Atg + Mt. ± Cb	mm-sized crystals (Ol1) + Ol2 polygons	7.38 ± 0.63, n = 15	1.77 ± 0.69, n = 18	−1.15 ± 1.04, $n = 4$
EK-Ol46 (LTG)	2′622′885, 1′090′470	Ol-vein crosscutting Ol-Atg-serpentinite	Ol + Atg + Mt. ± Cb ± Ti-Chu ± Di ± Chl	mm-cm sized Ol-crystals	5.81 ± 0.73, n = 19	1.22 ± 0.53, n = 17	n.a.
EK-Ol26 (LTG)	2′622′828, 1′090′405	Ol-vein crosscutting Ol-Atg-serpentinite	Ol + Atg + Mt. ± Ti-Chu ± Di ± Andr ± Prv	mm-cm sized Ol-crystals	n.a.	2.72 ± 0.80, n = 12	n.a.

$\delta^{18}O$ = oxygen isotopic composition, expressed in δ notation relative to the Vienna Standard Mean Ocean Water (V-SMOW). Values report the sample average ± 2SD, and additionally the number (n) of analyses per mineral phase.
Mt. = magnetite. All other mineral abbreviations follow Whitney and Evans (2010).
Samples with the prefix "EK" come from the collection of E.D. Kempf, while the other samples were collected for this study.

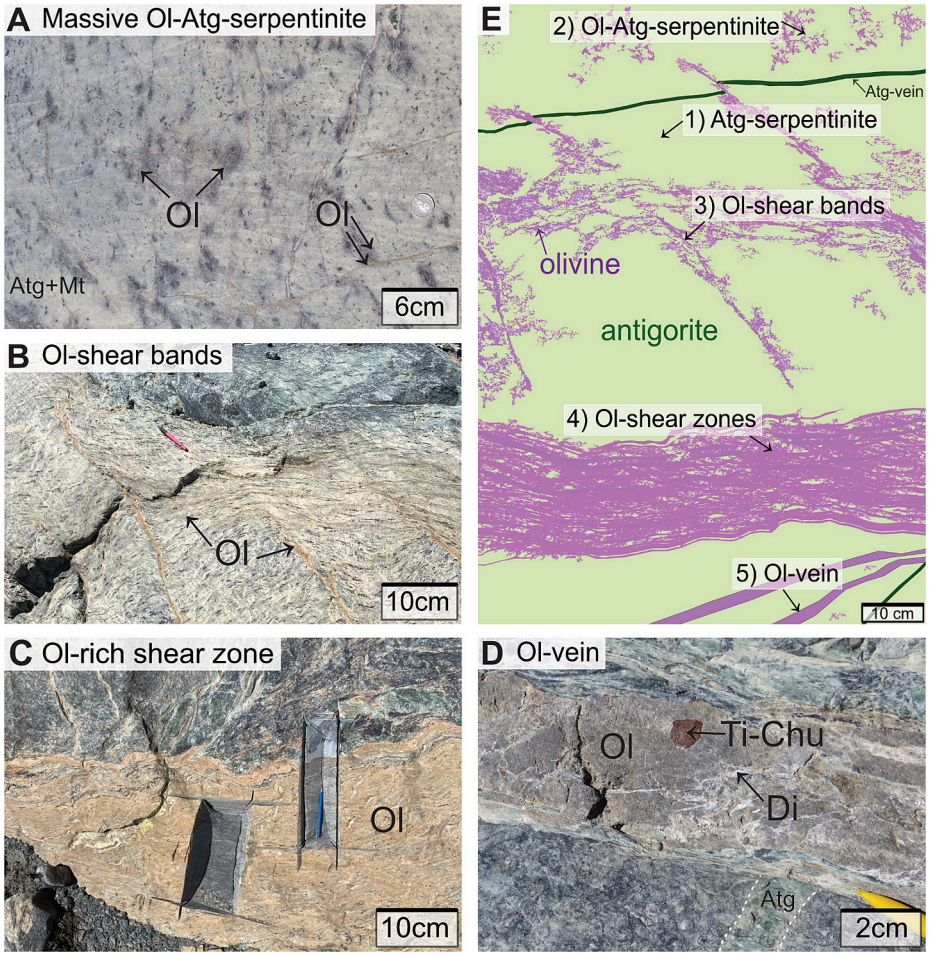

Fig. 2. Field photographs from the LTG and schematic representation of relationships and types of serpentinites collected for analysis based on the field observations. A) Massive Ol-Atg-serpentinite. B) Ol-shear bands, showing some thicker bands that are offset en-echelon (location of sample ZS-32). C) Ol-rich shear zone (sample EK-Ol1). Saw cuts indicate the location of sample EK-Ol1 (and -Ol2; which is not used for this study). D) Ol-vein (similar to sample EK-Ol46) cutting through Ol-Atg-serpentinite. E) Schematic representation of the field relationships between the different types of serpentinites.

are up to several mm in diameter (Fig. 3B), consisting of nearly pure Fe-magnetite with only rare Cr-magnetite rich cores. In the strongly foliated sample, antigorite occurs in flakes of about 30 × 100 μm with a strong preferred orientation. Magnetite forms mm-wide bands along the foliation, consisting of almost pure Fe-magnetite polygons (Fig. 3D).

Two nearly pure Atg-veins (samples ZS-19 and ZS-45, Fig. 3E) were collected at LTG to study antigorite that is not involved in the dehydration reaction that produced olivine. The vein antigorite is similar in size and texture to the antigorite in the Atg-serpentinites and forms patches of fine-grained antigorite within a coarser-grained antigorite matrix (Fig. 3F).

3.2. Ol-Atg-serpentinite, Ol-shear bands and Ol-veins

Metamorphic olivine occurs in four main textures (Fig. 2A–2E): (i) patches of olivine grown in pervasive replacement patterns in the massive Ol-Atg-serpentinites (Fig. 2A), (ii) olivine in shear bands (Fig. 2B), (iii) olivine in shear zones (Fig. 2C), and (iv) olivine in veins (Fig. 2D). Replacement olivine (Ol1) grows in large crystals in sample EK-FA and in sample ZS-40 (Fig. 2A and 4A). In these samples, the large mm-cm sized Ol1 crystals are cut by Ol-bands, consisting of smaller (50–200 μm) polygonal olivine grains (Ol2) that show a granoblastic texture (Fig. 4A). Antigorite is commonly present in fine-grained crystals of about 10 × 50 μm, or forms large flakes of about ~40 × 100 μm. Sample ZS-40 from UTG generally contains a higher abundance of antigorite and is more deformed compared to EK-FA. Further, the Ol2 polygons in sample ZS-40 are anhedral and elongated due to the stronger deformation at UTG than LTG.

Ol-shear bands are found in several samples from LTG and UTG (Table 1). The shear bands are several hundred μm to mm wide and consist mostly of Ol2 polygons (Fig. 4B and C), along with minor amounts of magnetite, antigorite and, in some samples, chlorite. Magnetite shows an equilibrium texture with olivine polygons, which is best observed in sample ZS-32 (Fig. 4C). In thicker shear bands (several mm to nearly cm thick), the core consists of larger olivine crystals, which may appear yellowish under the light microscope (Fig. 4C) due to fine Ti-clinohumite lamellae (see also De Hoog et al., 2014; Kempf et al., 2020). Some of these thicker shear bands are also displaced en-echelon (e.g., Fig. 2B). In all these samples, except for ZS-03 and EK-Ol1, antigorite is present in large flakes of up to ~30 × 100 μm. It either forms mm-wide bands between the Ol-shear bands, grows interlocked with the polygonal Ol2 of the Ol-band itself, or grows in round patches that are likely pseudomorphs of former orthopyroxene or mantle olivine (e.g., sample ZS-41; Fig. 4B). In sample ZS-03 and EK-Ol1, the modal abundance of antigorite is <20 vol% as these samples represent Ol-rich shear zones (Fig. 2C). Antigorite occurs as single blades of ~40 μm x ~ 150 μm next to olivine, or is only concentrated in Ol-free bands or pockets, which are surrounded by olivine polygons. Sample ZS-03 is also cut by an approximately 500 μm wide calcite-dolomite vein (confirmed by Raman spectroscopy).

Ol-veins, represented by samples EK-Ol26 and EK-Ol46, are cm to dm wide. The olivine veins are composed of up to ~90 vol% metamorphic

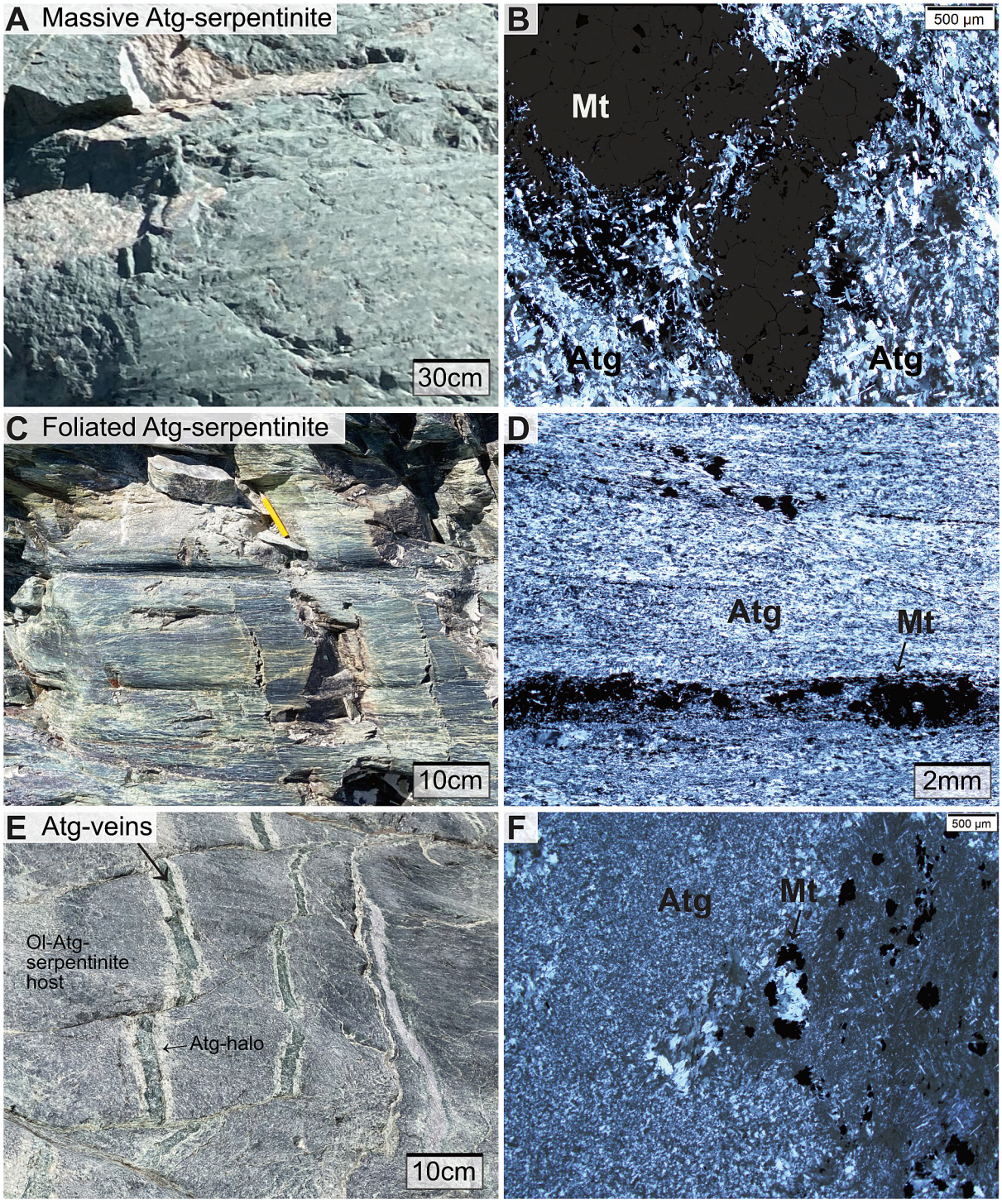

Fig. 3. Atg-serpentinite and Atg-vein samples. A) Outcrop of a massive Atg-serpentinite from LTG. The striated pattern is due to the glacial polishing. B) Photomicrograph (cross-polarized light) of sample ZS-18 showing magnetite polygons in a coarse-grained Atg-matrix. C) Outcrop of the strongly foliated Atg-serpentinite ZS-02 from UTG. D) Photomicrograph (cross-polarized light) of sample ZS-02 showing bands of magnetite within the antigorite foliation. E) Outcrop from LTG with Atg-veins cutting the Ol-Atg-serpentinite host. At the contact between some veins and the host rock, the serpentinite is recrystallized and olivine and magnetite are no longer present, appearing as white-greenish halos. F) Photomicrograph (cross-polarized light) of Atg-vein ZS-19 showing finer and coarser grained antigorite domains.

olivine with minor antigorite, Ti-clinohumite, metamorphic diopside, magnetite and calcite (Figs. 2D and 4D). Olivine crystals are large (mm up to cm) and appear dusty due to numerous inclusions of opaque minerals. Antigorite is present in large flakes, and it often surrounds the olivine crystals together with calcite (Fig. 4D). Sample EK-MF4, which contains a narrow olivine vein <1 cm in diameter, is referred to as a veinlet, and it is distinct from the cm-dm wide Ol-veins. Its mineral assemblage is the same as that of the Ol-shear bands.

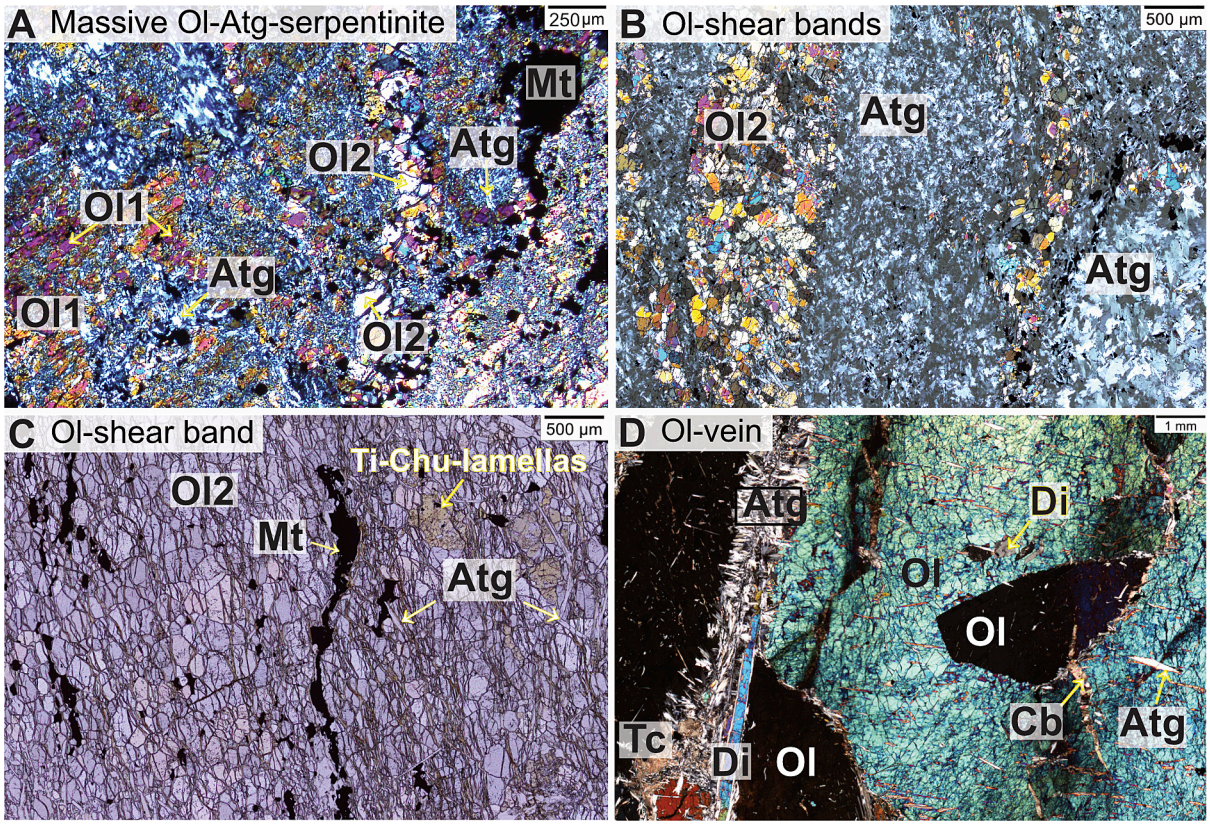

Fig. 4. A) Photomicrograph (cross-polarized light) of massive Ol-Atg-serpentinite EK-FA showing a texture of antigorite and large Ol1 cut by Ol2 bands. B) Photomicrograph (cross-polarized light) of Ol2 polygons in shear bands in sample ZS-41. C) Photomicrograph of Ol2 polygons in a thicker en-echelon shear band in sample ZS-32 (outcrop photo with en-echelon shear bands shown in Fig. 2B). Ti-clinohumite (Ti-Chu) lamellas are intergrown with Ol2. D) Photomicrograph (cross-polarized light) of Ol-vein EK-Ol46 showing large olivine crystals with inclusions of single blades of antigorite.

4. Analytical methods and modeling approach

4.1. Electron microprobe analysis (EPMA)

Major elements in olivine, antigorite and magnetite were measured using a JEOL JXA-8200 electron probe micro analyzer (EPMA) at the Institute of Geological Sciences, University of Bern. Quantitative spot analysis, X-ray mapping and backscattered electron (BSE) imaging were used to study the different microtextures of the samples. The acceleration voltage for spot analysis was 15 kV with a probe current of 20 nA and a measurement time of 20 s at the peak and 10 s at the background positions on either side of the peak. The following reference materials were used to calibrate the chemical elements analyzed: anorthite (Al, Ca; on TAP and PETL analyzer crystals, respectively), orthoclase (Si; on TAP), magnetite (Fe; on LIFH), forsterite (Mg; on TAP), chromium spinel (Cr; on PETL), tugtupite (Cl; on PETH), rutile (Ti; on PETJ), pyrolusite (Mn; on PETL) and bunsenite or a Ni-alloy (Ni; on LIFH). X-ray mapping was performed with a probe current of 100 nA, a dwell time between 200 and 300 ms and a pixel size of 3–5 µm. The acquired X-ray maps were quantified with previously measured spots in the map area and were further processed and calibrated using the XMapTools software (Lanari et al., 2014, 2019).

4.2. Laser ablation inductively coupled mass spectrometry (LA-ICP-MS)

Minor and trace elements were measured by LA-ICP-MS using a RESOlutionSE 193 nm excimer laser system coupled to an Agilent 7900 quadrupole ICP-MS at the Institute of Geological Sciences, University of Bern. SRM-NIST 612 glass was used to optimize the mass spectrometer at a low oxide production rate of $ThO^+/Th^+ < 0.3\%$. The laser repetition rate was set to 5 Hz with an on-sample fluence of 3 $J{\cdot}cm^{-2}$ and 4 $J{\cdot}cm^{-2}$ for antigorite and olivine, respectively. The beam size was 50 µm and the acquisition time for each measurement was ~30 s for background and ~30 s for sample. For minor and trace elements, primary standard USGS-GSD-1G and secondary standard SRM-NIST 612 were analyzed every 10 unknowns. Data reduction was performed using the IOLITE software (Hellstrom et al., 2008; Paton et al., 2011) with GSD-1G glass as the external standard by using values reported in Peters and Pettke (2017), and Mg concentrations from quantitative EPMA analysis on minerals as the internal standard. For magnetite, Fe concentrations were used as the internal standard instead of Mg. In absence of a serpentine or olivine mineral reference material, the measurement accuracy was monitored by measuring SRM-NIST 612 as unknown. Accuracy, expressed as deviation from the accepted values reported in the GeoReM database as of Dec09 (Jochum et al., 2007), is for most elements better than 10% with ~1–2% for Li, Rb, Nb and Ba, ~1–5% for Ti, Ni, Sb, Tm, W and Th, and ~5–10% for Sc, V, Cr, Mn, Co, Zn, Sr, Zr, La, Ce, Pr, Nd, Sm, Dy, Ho, Yb, Lu, Pb and U. Exceptions are B (~19%), As (~29%), Gd (~16%) and the elements Y, Eu, Tb and Er (~10–15%).

4.3. Secondary ion mass spectrometry (SIMS)

The in-situ O isotope measurements were performed with a Cameca IMS 1280 HR ion microprobe at the SwissSIMS facility (University of Lausanne, Switzerland) and, for a few samples, at the CRPG-CNRS (Nancy, France), with the same analytical conditions. The Cs^+ primary ion beam current was ~1.5–2.0 nA with an acceleration voltage of 20 kV (+10 kV/ -10 kV) and was focused to a diameter of ~20 µm with a Gaussian density distribution. $^{16}O^-$ and $^{18}O^-$ secondary ions were simultaneously measured by multicollection on Faraday cups. Each

analysis took ~3 min, or ~5 min including 90 s background measurements at CRPG-CNRS respectively, including 30 s pre-sputtering, and automatic centering of the secondary ions, and analysis over 20 cycles. O isotope compositions are expressed in δ notation relative to the Vienna Standard Mean Ocean Water (V-SMOW).

Three different matrix-matched reference materials were used to correct for instrumental mass fractionation (IMF): San Carlos olivine ($\delta^{18}O = +5.27 \pm 0.1$ ‰, 2σ; Eiler et al., 1995), Al06-44A antigorite ($\delta^{18}O = +8.3 \pm 0.1$ ‰, 2σ; Scicchitano et al., 2018), and Charoy magnetite ($\delta^{18}O = +5.7 \pm 0.2$ ‰, 2σ; in-house reference material at CRPG-CNRS, University de Lorraine, Nancy). Typical internal uncertainties for individual analyses of reference materials and samples are 0.1–0.2 ‰ (2se), independent of the mineral. The repeatability of the reference material varied for each analytical session from ~0.2–0.5 ‰ (2σ) for SCO, from ~0.3–0.6 ‰ for Al06-44A , and from ~0.4–0.6 ‰ for Charoy magnetite (within single grain for magnetite). Therefore, the final uncertainty on the corrected $\delta^{18}O$ values is no less than the repeatability of the reference materials for each session.

It is known that for some minerals, variations in their composition, mainly the Fe vs. Mg content, can significantly change the IMF. For olivine, it has been reported that the IMF does not change significantly between Fo70–Fo100, while for the Fe-rich olivine, the IMF changes drastically between Fo0–Fo70 (e.g., Isa et al., 2017; Scicchitano et al., 2018b). To determine a possible matrix effect between San Carlos olivine (Mg# of 89.7) and the studied olivine (Mg# of 94–96), seven olivine reference materials with different forsterite contents (VS24A = $Fo_{73.8}$, VS4 = $Fo_{76–77}$, VS18 = $Fo_{78.7}$ from Tollan et al., 2012, SCO = $Fo_{89.7}$, Eiler et al., 1995, and Fo94 = Fo_{94}, JUB = $Fo_{99.7}$ and SF100 = Fo_{100} from Scicchitano et al., 2018b) were analyzed within one SIMS session. For all these reference materials within a forsterite content of Fo70 to Fo100, no significant change in IMF was observed (± 0.6 ‰, 2σ; Supplementary Table S1).

For antigorite, the study by Scicchitano et al. (2020) showed that the relative bias between the antigorite reference materials with different Mg/Fe ratios is about 1.8 ‰ for the range in Mg# of ~78–100, described by a second-order polynomial. The antigorite reference material Al06-44A has an Mg# of ~94–95, while the studied antigorite from Zermatt-Saas has an Mg# of ~96–98, resulting in only a small bias in the order of ~0.1–0.3 ‰, which is within the analytical uncertainty.

Besides matrix effects, channeling and tunneling of ions can lead to variations in the measured oxygen isotope ratio by SIMS for some minerals, depending on the orientation of their crystal structure with respect to the incident ion beam. Minerals known for their orientation effect in SIMS are $\delta^{18}O$ in hematite (Huberty et al., 2010; White et al., 2021) and $\delta^{34}S$ in sphalerite and galena (Kozdon et al., 2010), while the orientation effect of magnetite on $\delta^{18}O$ is controversial (e.g., Lyon et al., 1998; Kita et al., 2010; Huberty et al., 2010; Marin-Carbonne et al., 2011). Huberty et al. (2010) reported a bias in $\delta^{18}O$ of 2–3 ‰ due to orientation effects by using the same instrument employed for this study (Cameca IMS-1280). The recent study by Scicchitano et al. (2022) demonstrated a grain-to-grain reproducibility of ~1 ‰ on randomly oriented M7–5830 magnetite reference material, using a special low-kV protocol (Kita et al., 2010; Huberty et al., 2010). During an analytical session in our study, different kV protocols were applied with no improvement in reproducibility. Therefore, the 20 kV protocol was used to analyze magnetite, olivine, and antigorite within the same session.

In this study only Fe-rich magnetite analyses were considered whereas texturally older Cr-rich magnetite cores, which have higher measured $\delta^{18}O$ values of approximately +3 to +5 ‰, are discarded because of a potential Cr—Fe matrix bias relative to the Fe-rich reference material.

4.4. Isotope fractionation modeling

A combined approach between thermodynamic and oxygen isotope fractionation modeling (Vho et al., 2019; Lanari and Duesterhoeft, 2019) is used to quantify isotopic equilibrium fractionation and to compare the measured $\delta^{18}O$ values with the modeled $\delta^{18}O$ values. The program ThorPT, developed in-house, is used to model the evolving stable phase assemblage and oxygen isotope fractionation, following the approach of the program PTLoop (Vho et al., 2020) Theriak-Domino is used for Gibbs Free Energy minimization, using the internally consistent dataset tc55 of Holland and Powell (1998) with subsequent updates from Kempf et al. (2020) to model the stable phase assemblage and the fluid production (approach after Lanari and Duesterhoeft, 2019) along a given P–T trajectory (prograde P–T path from Bovay et al., 2021). The model uses the major element composition of the sample of interest as input. Two representative bulk rock compositions were used for the modeling: Rock 1 (sample EK-FA) from local bulk rock composition extracted from EPMA maps (approach following Lanari and Engi, 2017), and Rock 2 (sample lg50) from slightly modified XRF data from Li et al. (2004). The bulk compositions were simplified to the $MgO–FeO–Al_2O_3–SiO_2–H_2O$ system, are water saturated, and no Fe^{3+} was considered in the calculations. The calculations use the solution models of Holland and Powell (1998) for olivine, orthopyroxene and brucite; Holland et al. (1998) for chlorite; and the Al-Tschermak exchange model of Padrón-Navarta et al. (2013) for antigorite. The new solid solution model for antigorite and lizardite endmembers by Eberhard et al. (2023), which accounts for Fe^{3+} and Al-Tschermak exchange, is not yet implemented in the current version of ThorPT.

The program ThorPT also uses a given $\delta^{18}O$ bulk composition and the internally consistent database DBOXYGEN version 2.0.3 (Vho et al., 2019) to model oxygen isotope fractionation among the predicted stable phases as a function of temperature. Antigorite separates from the Zermatt-Saas area have $\delta^{18}O$ values of +3 to +6 ‰ (e.g., Seydoux and Baumgartner, 2013; Widmer, 1996; Cartwright and Barnicoat, 1999). The separates do not contain olivine, which would have a lower $\delta^{18}O$ than antigorite at equilibrium, and thus a lower bulk $\delta^{18}O$ value of +3 ‰ was taken to best represent the samples analyzed in this study. Further modeling details (e.g., also modeling with a $\delta^{18}O$ bulk composition of +5 ‰) can be found in the supplementary material S4.

5. Results

5.1. Mineral chemistry

Major, minor and trace element compositions of antigorite, olivine and magnetite were measured in this study (Supplementary Table S2). Further data on the composition of minor phases such as chlorite, diopside, Ti-clinohumite, Ti-chondrodite, andradite-uvarovite garnet, ilmenite, and perovskite from LTG samples are published in Kempf et al. (2020).

5.1.1. Antigorite

Antigorite in massive serpentinites, and antigorite in strongly foliated serpentinites show no significant differences in major element composition. Antigorite in Atg-serpentinites, in Atg-veins, and antigorite coexisting with olivine show only minor variations in Mg# between 97 and 98. Their Al_2O_3 and Cr_2O_3 contents vary between 0.4 and 2.1 wt% and 0.1–0.6 wt%, respectively. In some samples from both UTG and LTG, Al zonation within individual antigorite blades could be detected by EMPA mapping (e.g., antigorite in sample ZS-03, Fig. 5A and B). Aluminum concentration in antigorite formation via Tschermak substitution is temperature dependent when the Al content is buffered by another Al phase such as chlorite (Padrón-Navarta et al., 2008, 2013). Therefore, the variation in Al concentration within individual blades in samples that also contain chlorite (e.g., ZS-03, EK-FA, EK-Ol1) suggests antigorite formation at different P-T conditions.

Antigorite also shows no deformation-dependent minor and trace element variations, and antigorite is depleted in most elements compared to the primitive mantle, except for Sc and Cr, which are comparable to the primitive mantle, and the fluid mobile elements B, As

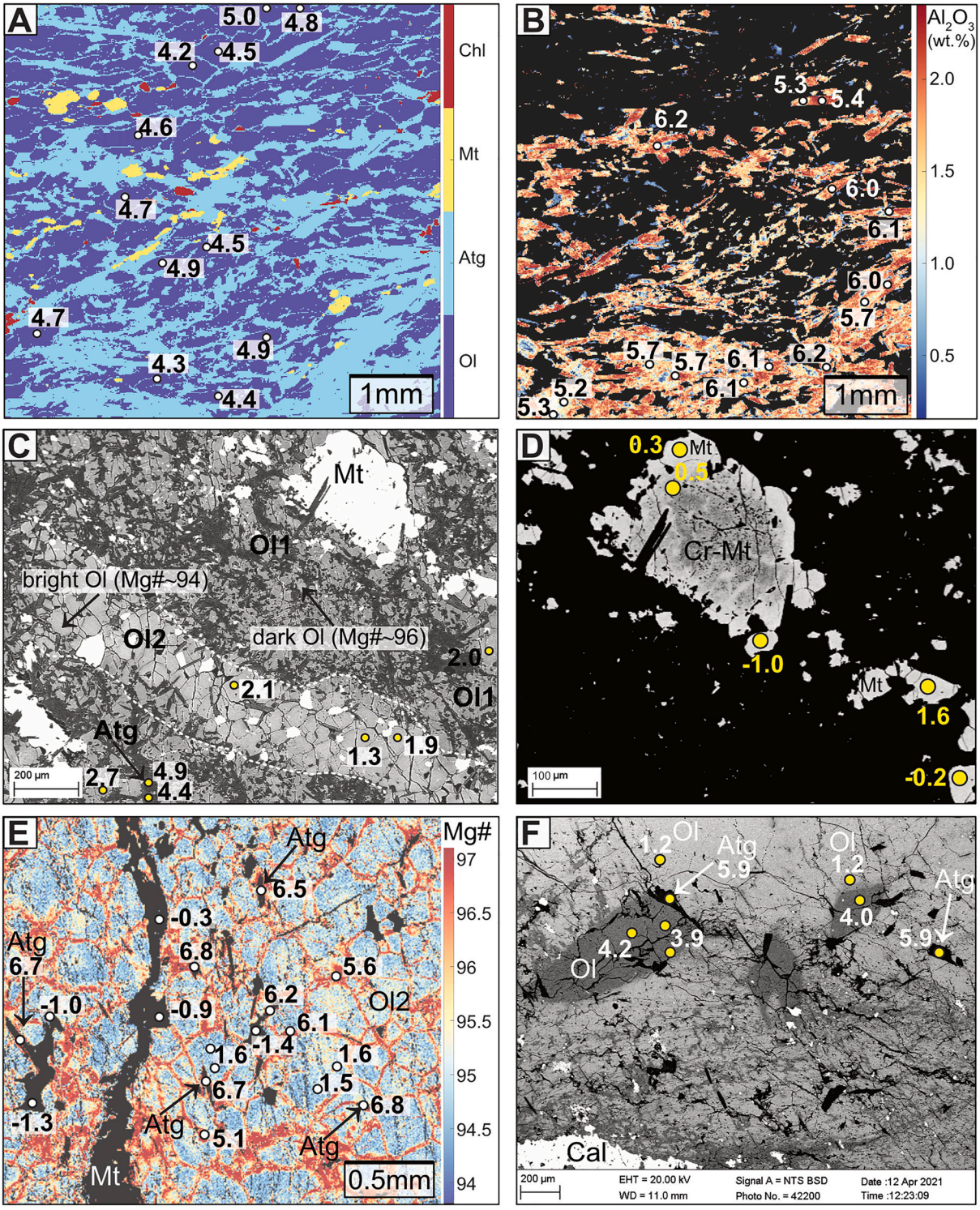

Fig. 5. Microtextures (BSE images and elemental maps) with SIMS $\delta^{18}O$ measurements (white or yellow circles, values in ‰) in antigorite (Atg), olivine (Ol) and magnetite (Mt). A) EPMA phase map of sample ZS-03 obtained with XMapTools 4.2 (Lanari et al., 2019). $\delta^{18}O$ values are reported for olivine only. B) EPMA map of Al in sample ZS-03 showing zoning in antigorite. $\delta^{18}O$ values are reported for antigorite only. Black areas are mainly olivine. C) BSE image showing differences in Mg# between Mg-rich Ol1 crystals (dark Ol) and crosscutting Fe-rich polygonal Ol2 (bright Ol) in sample EK-FA. Dark gray flakes are antigorite and white crystals are magnetite. D) Fe-rich magnetite with Cr-magnetite core in sample EK-FA. E) EPMA map of sample ZS-32 showing Ol2 polygons ($\delta^{18}O \sim +2$ ‰) with Mg-rich rims ($\delta^{18}O \sim +5$ ‰). High Mg# zones were checked with BSE to confirm the location of $\delta^{18}O$ and EPMA analyses in clean olivine and the elemental map was filtered for olivine. F) BSE image showing differences in Mg# between vein olivine (Mg# = 94–95, $\delta^{18}O \sim +1$ ‰, light gray) and texturally later olivine along fractures (Mg# = 97–98 and $\delta^{18}O \sim +4$ ‰, dark gray) where magnetite is also present (bright zones). Black flakes are antigorite. (For interpretation of the references to colour in this figure legend, the reader is referred to the web version of this article.)

and Sb, which are enriched compared to the primitive mantle (Fig. 6A). Interestingly, As and Sb concentrations in antigorite differ between LTG and UTG samples (Fig. 7). LTG samples are enriched in As and Sb (1–25 µg/g and 0.5–5 µg/g, respectively) compared to the UTG samples (0.03–5 µg/g and ~ 0.1 µg/g or below detection, respectively), and As and Sb in antigorite are positively correlated (Fig. 7B). The concentration of B, on the other hand, is roughly comparable between the two outcrop parts, ranging from 4 to 28 µg/g. However, within each outcrop part, B in antigorite is positively correlated with As, and thus Sb (Fig. 7A).

5.1.2. Olivine

Olivine from all samples examined shows no deformation-related variations in its major element composition and has a high Mg# of 94–96, except for sample ZS-43 from UTG, which has a Mg# of 92. While olivine is generally homogeneous in composition in most samples from both outcrop parts, some minor zoning is observed. The Ol1 generation (e.g., in samples EK-MF4 and EK-FA) is generally Mg richer than the Ol2 polygons (Fig. 5C). Another slight difference in Mg# is present at the rims of the Ol2 polygons (e.g., for sample ZS-32; Fig. 5E) and along fractured and recrystallized olivine in the Ol-vein of sample EK-Ol46. The recrystallized domains appear darker than the surrounding vein olivine in BSE images and have an Mg# of 98 (Fig. 5F).

The minor and trace element composition of olivine is depleted for most elements compared to the primitive mantle. Similar to antigorite, olivine is enriched in B, As and Sb (in UTG samples, Sb in olivine is below the detection limit). The concentration of Co, Ni and Zn for a few LTG samples is similar to that of the primitive mantle, while Mn is slightly enriched (Fig. 6B). As, Sb and additionally B in olivine are different for the two outcrop parts (Figs. 6B and 8A). Olivine from LTG samples is richer in As (0.2–4.0 µg/g) and Sb (0.02–0.07 µg/g), but poorer in B (~6–9 µg/g) compared to the UTG samples (As ~0.02–0.03 µg/g or below the detection limit; Sb is always below the detection limit; B ~ 11–84 µg/g). Olivine from UTG samples shows a positive correlation between B—As and deformation, with olivine grown by pervasive replacement having the lowest B and As concentrations, and olivine in shear zones having the highest B and As concentrations (Fig. 8A). In contrast, olivine from LTG samples shows only a positive correlation between As content and texture, with vein olivine having higher As concentrations than olivine in massive serpentinites. Boron concentrations, however, remain the same over the different olivine textures analyzed (Fig. 8A).

5.1.3. Magnetite

Magnetite from all samples is relatively homogeneous in its major element composition and is Fe-rich with low Cr_2O_3 (0.3–4.2 wt%) and MgO (1.1–4.1 wt%; Table S2). In most samples, some of the Fe-rich magnetite contain older, Cr-rich cores (Fig. 5D), and samples ZS-03 and ZS-25 also host mantle relic Cr-spinel.

Minor and trace elements for magnetite are generally depleted

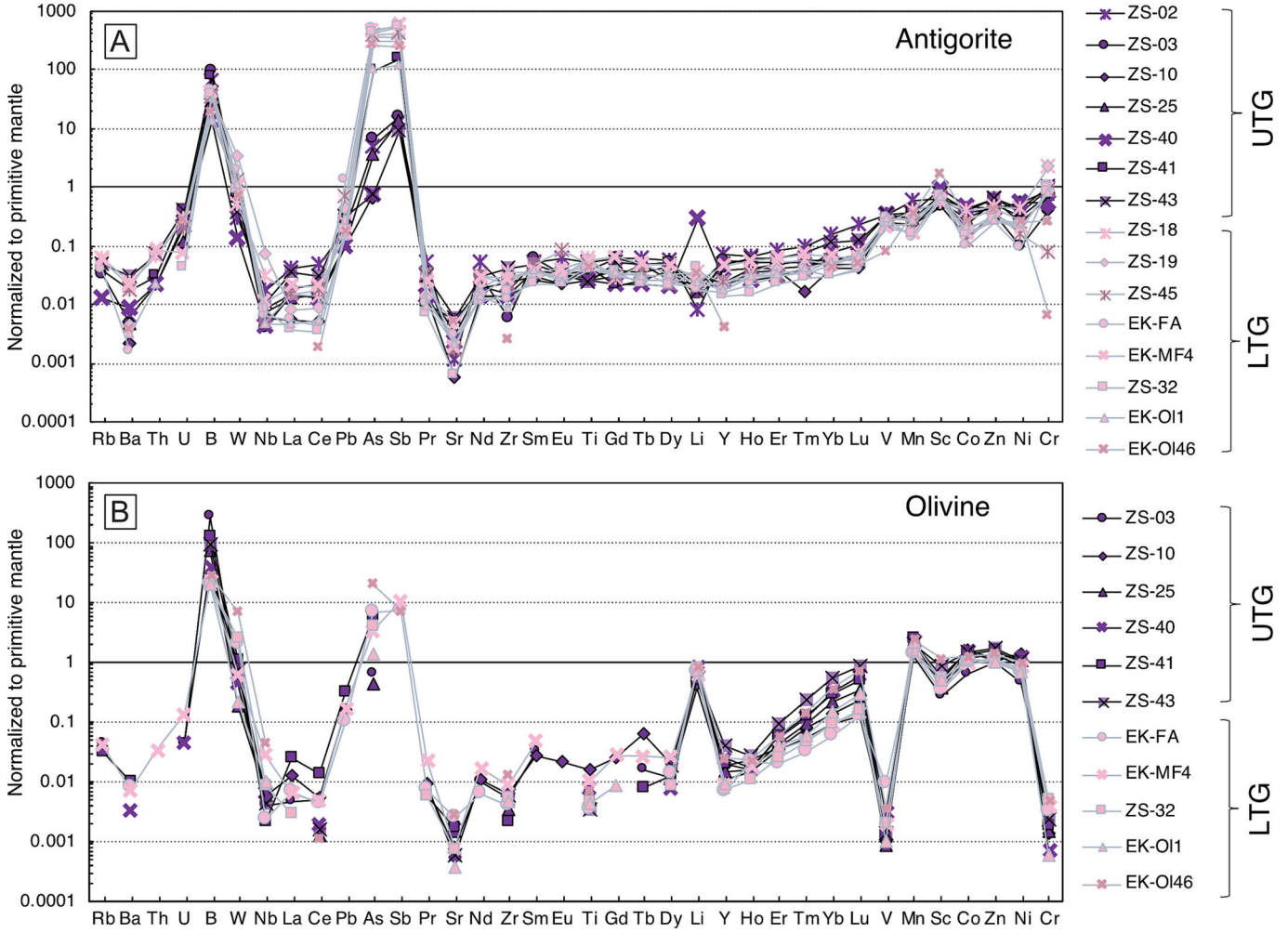

Fig. 6. A) Antigorite and B) olivine minor and trace element patterns for UTG and LTG samples. Each pattern represents the average composition of multiple LA-ICP-MS spot analyses. An exception is olivine from sample EK-MF4, where the median values better represent the minor and trace element composition. Values are normalized to the primitive mantle compositions of McDonough and Sun (1995).

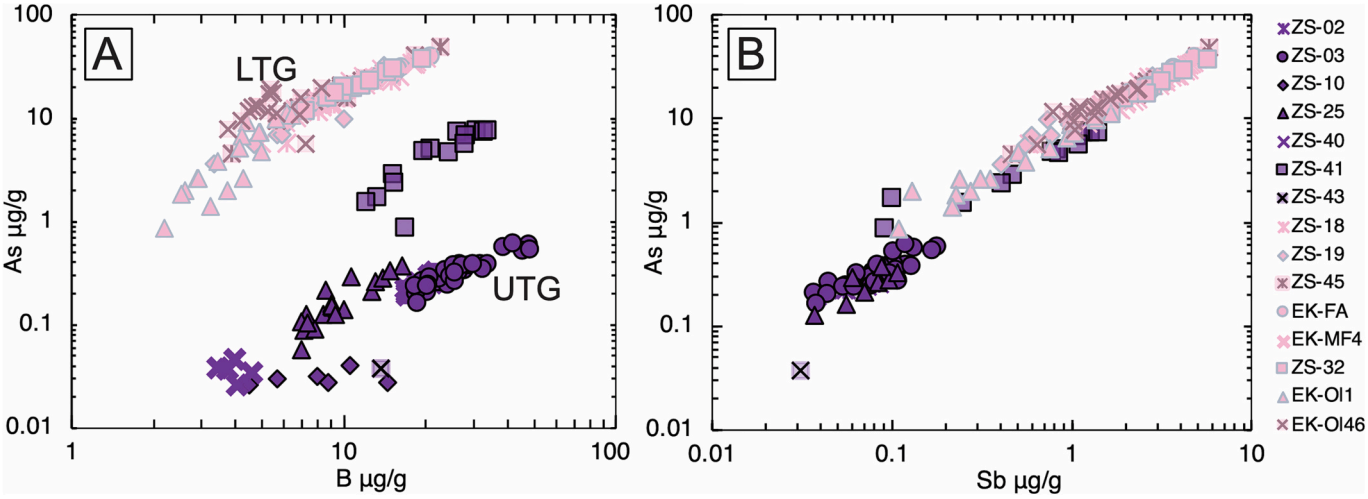

Fig. 7. Bivariate plots highlighting the differences in fluid-mobile element concentrations in antigorite between the UTG and LTG samples: A) As vs. B and B) As vs. Sb. This difference is attributed to the different serpentinization conditions of the protoliths (see text).

compared to the primitive mantle, but enrichments for V, Cr, Mn, Zn, As and Sb are found (only samples EK-FA and EK-Ol26 were analyzed for magnetite, Table S2). The composition of magnetite in the Zermatt-Saas samples is comparable to that of magnetite from the Almirez Atg-serpentinites (Vieira Duarte et al., 2021).

5.2. Oxygen isotopic compositions

$\delta^{18}O$ values standardized to matrix-matched reference materials of antigorite, olivine, and magnetite from the Zermatt-Saas serpentinites are given in Table 1 and plotted in Fig. 9. Additional information on individual measurements, including reference materials, is given in Supplementary Tables S1 and S3.

5.2.1. Antigorite

The average oxygen isotopic composition of antigorite in individual samples ranges from a $\delta^{18}O$ of +3.5 ± 0.9 ‰ to +8.4 ± 1.6 ‰ (2σ). Two distinct compositional groups are present: antigorite with low $\delta^{18}O$ of +3.5 to +4.2 ‰ and antigorite with high $\delta^{18}O$ of +5.5 to +8.4 ‰. Both groups of antigorite are found in samples from UTG and LTG, although the antigorite from LTG is dominated by high $\delta^{18}O$ values. No correlation is found between these two isotopic groups and the antigorite texture or the degree of deformation within the sample (antigorite in massive or foliated samples). Within both outcrop parts, but more pronounced at UTG with the larger inter-sample variability in the $\delta^{18}O$ of antigorite, the samples with higher $\delta^{18}O$ values (samples ZS-02, ZS-03 and ZS-41) also have higher B concentrations (~30 µg/g) than samples with lower $\delta^{18}O$ values (~6–11 µg/g in samples ZS-40, ZS-43, ZS-10, and ZS-25; S5).

5.2.2. Olivine

Olivine has a fairly homogeneous $\delta^{18}O$ over the km scale at both outcrop parts (UTG and LTG) with low values of +1.2 to +2.5 ‰ for pervasively replaced Ol1 in the massive Ol-Atg-serpentinites as well as for Ol2 polygons in Ol-shear bands and Ol-veins. A minority of samples at both sites also contain olivine with higher $\delta^{18}O$ values of +3.8 to +5.5 ‰. The isotopically heavier olivine occurs either as Ol2 or as texturally late olivine at rims and along fractures. In samples from LTG, the isotopically heavier olivine is texturally late, has higher Mg# (up to 98), and occurs only at the rims of low $\delta^{18}O$ olivine grains (sample ZS-32, Fig. 5E) or along fractures (sample EK-Ol46, Fig. 5F). The isotopically heavier olivine in samples from UTG is not associated with texturally later growth at rims or along fractures, but olivine cores and rims of Ol2 share the same high $\delta^{18}O$ (e.g., sample ZS-03). Similar to antigorite in the section above, samples with higher $\delta^{18}O_{Ol}$ also have higher B concentrations in olivine than samples with lower $\delta^{18}O_{Ol}$ (see S5).

In contrast to samples from LTG, samples from UTG contain isotopically heavy olivine ($\delta^{18}O$ of +3.8 to +4.6 ‰) coexisting with high $\delta^{18}O$ antigorite (+5.5 to +6.3 ‰), and isotopically light olivine ($\delta^{18}O$ of +1.8 to +2.5 ‰) occurs only in the presence of low $\delta^{18}O$ antigorite (+3.5 to +4.1‰) (Fig. 9A).

5.2.3. Magnetite

Magnetite generally has a negative $\delta^{18}O$ value of about −1 ‰ in most of the samples analyzed. However, there is considerable within-sample variability, which may be due to orientation effects during SIMS measurements (see Section 4.3). Magnetite in two UTG samples (ZS-02 and ZS-03) has significantly higher $\delta^{18}O$ values of +1 to +2 ‰. These two samples also have correspondingly high $\delta^{18}O$ antigorite, and in the case of sample ZS-03, relatively high $\delta^{18}O$ olivine.

5.3. Isotope fractionation modeling

Results for the modeled evolving stable phase assemblage, fluid release, and the oxygen isotope fractionation for two representative bulk rock compositions are displayed in Fig. 10. The stable phases predicted by the model are slightly different for the two bulk rock compositions, because Rock 2 also has chlorite stable compared to Rock 1 (Fig. 10A and C). The amount of fluid released is also different, with Rock 1 releasing >4 vol% of fluid and Rock 2 releasing ~2.5–3.0 vol% of fluid (Fig. 10A and C). The model-predicted phases of samples containing mainly antigorite and olivine ± chlorite match the observed phases, except for magnetite. Magnetite is not stabilized in the model because no Fe^{3+} was considered in the calculations, but in the natural samples, magnetite is always present. Forcing the model to stabilize magnetite by artificial addition of Fe^{3+} as Fe_2O_3 does not change the predicted fluid release (given in vol%) or the oxygen isotope fractionation (see S4). Similarly, the prediction of chlorite for the stable phase assemblage of Rock 2 has little effect on the isotopic fractionation between antigorite, olivine and released fluid (Fig. 10B and D).

Given an initial bulk $\delta^{18}O$ of +3 ‰, the model predicts for Rock 1 and Rock 2 antigorite with $\delta^{18}O$ values of about +3 to +4 ‰, coexisting with $\delta^{18}O_{Ol}$ of +1 to +2 ‰ at peak reaction temperatures (525–550 °C, Fig. 10B and D). If magnetite is stabilized (S4), it would have a $\delta^{18}O$ of −1 ‰ between 525 and 550 °C. These predicted peak reaction temperatures are slightly lower than the suggested peak temperatures of 550–600 °C by Kempf et al. (2020).

Kempf et al. (2020) suggested the shift from the modeled

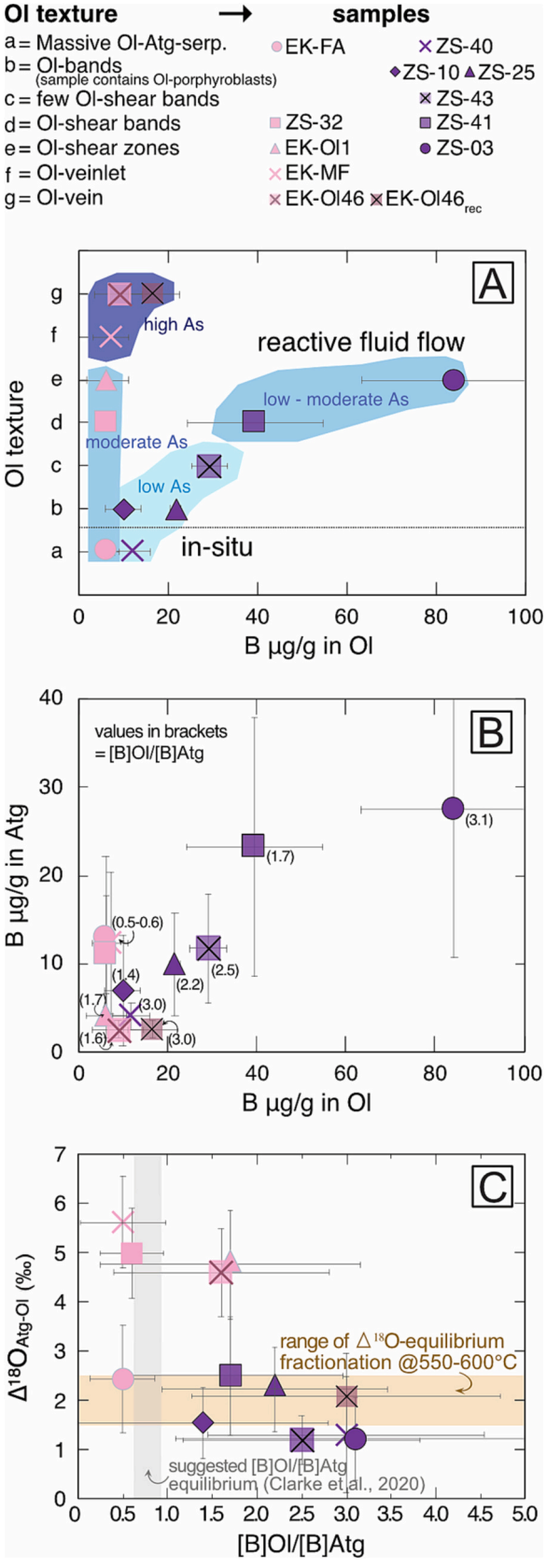

(caption on next column)

Fig. 8. Comparison between Ol texture, boron concentration, [B]Ol/[B]Atg and $\Delta^{18}O_{Atg\text{-}Ol}$. B concentration, [B]Ol/[B]Atg and $\Delta^{18}O_{Atg\text{-}Ol}$ values are given as sample averages with uncertainty (2SD). Light purple symbols represent LTG samples and dark purple symbols represent UTG samples. A) Boron concentration in olivine with textural evolution from in-situ produced olivine in a massive Ol-Atg-serpentinite to olivine in Ol-shear bands, Ol-shear zones and Ol-veins. B) Boron concentration in olivine vs. antigorite and [B]Ol/[B]Atg values. C) [B]Ol/[B]Atg values vs. $\Delta^{18}O_{Atg\text{-}Ol}$. The orange horizontal band illustrates the $\Delta^{18}O_{Atg\text{-}Ol}$ equilibrium fractionation, and the vertical gray band illustrates the [B]Ol/[B]Atg equilibrium, suggested by Clarke et al. (2020). (For interpretation of the references to colour in this figure legend, the reader is referred to the web version of this article.)

temperatures of ~525–550 °C to higher temperatures of 550–600 °C based on olivine Mg#, Al-in-olivine thermometry, and (Al + Cr)# in antigorite.

The difference in the calculated oxygen isotope fractionation due to this minor temperature difference is very small, below the precision of the SIMS $\delta^{18}O$ measurements. Therefore, the temperature range of 550–600 °C is considered being valid for the peak brucite+antigorite dehydration reaction, and this temperature range is used for the isotope fractionation calculations and discussion.

6. Discussion

It has been shown that in the Zermatt-Saas HP ophiolite (e.g., Kempf et al., 2020; Clarke et al., 2020) metamorphic olivine and aqueous fluid are produced by the dehydration reaction of brucite + antigorite (Ulmer and Trommsdorff, 1995; Scambelluri et al., 2004a; Kempf et al., 2020). The amount of olivine in nearly undeformed serpentinites produced by this reaction depends on the amount of brucite formed during oceanic alteration. This parameter can only be constrained by calculations using bulk rock compositions, as relict brucite is not present in the Zermatt-Saas serpentinites (Kempf et al., 2020). The distribution of olivine shows considerable variability at both outcrop and thin-section scales. The modal abundance of olivine in Ol-shear bands, Ol-shear zones, and Ol-veins is particularly high (Figs. 2D and 4D), exceeding the amount that can be produced in situ by the reaction alone, assuming a reasonable amount of brucite (7–17 wt%, Kempf et al., 2020). This finding suggests that olivine production is not exclusively in situ for all samples, but is the result of another process that concentrates and forms olivine. Trace elements and oxygen isotope fractionation between newly formed olivine, coexisting antigorite and magnetite may reveal differences in the formation process and provide further insight into serpentinization conditions prior to the dehydration reaction.

Using the combined approach of trace element and oxygen isotope systematics, the following aspects are discussed: (1) the heterogeneity of serpentinites due to serpentinization conditions; (2) the behavior of oxygen isotopes during the transition from oceanic to subducted serpentinites; (3) the formation processes of metamorphic olivine revealed by oxygen isotopic equilibrium vs. disequilibrium with the coexisting antigorite and magnetite, including the oxygen isotope fractionation modeling; and (4) the isotopic signature of the fluids released and the fluid pathways.

6.1. *Variable serpentinization conditions*

Based on Cr# versus Mg# in the relic spinel, it has been suggested that the Zermatt-Saas ophiolite is derived from a precursor harzburgite and was serpentinized in a setting at or near mid-ocean ridges, such as the Atlantis Massif (e.g., Kempf et al., 2020; Hellebrand et al., 2001 and 2002; Vils et al., 2008; Barnes et al., 2014). Serpentinites formed in such settings are typically enriched in B, As, Sb, U, W, Cl, Br, I, Sr, Li and LILE when compared to the primitive mantle (e.g., Kodolányi et al., 2012; Vils et al., 2008; Savov et al., 2005, 2007; Deschamps et al., 2011; Scambelluri et al., 2004a; Peters et al., 2017, 2020). During subduction,

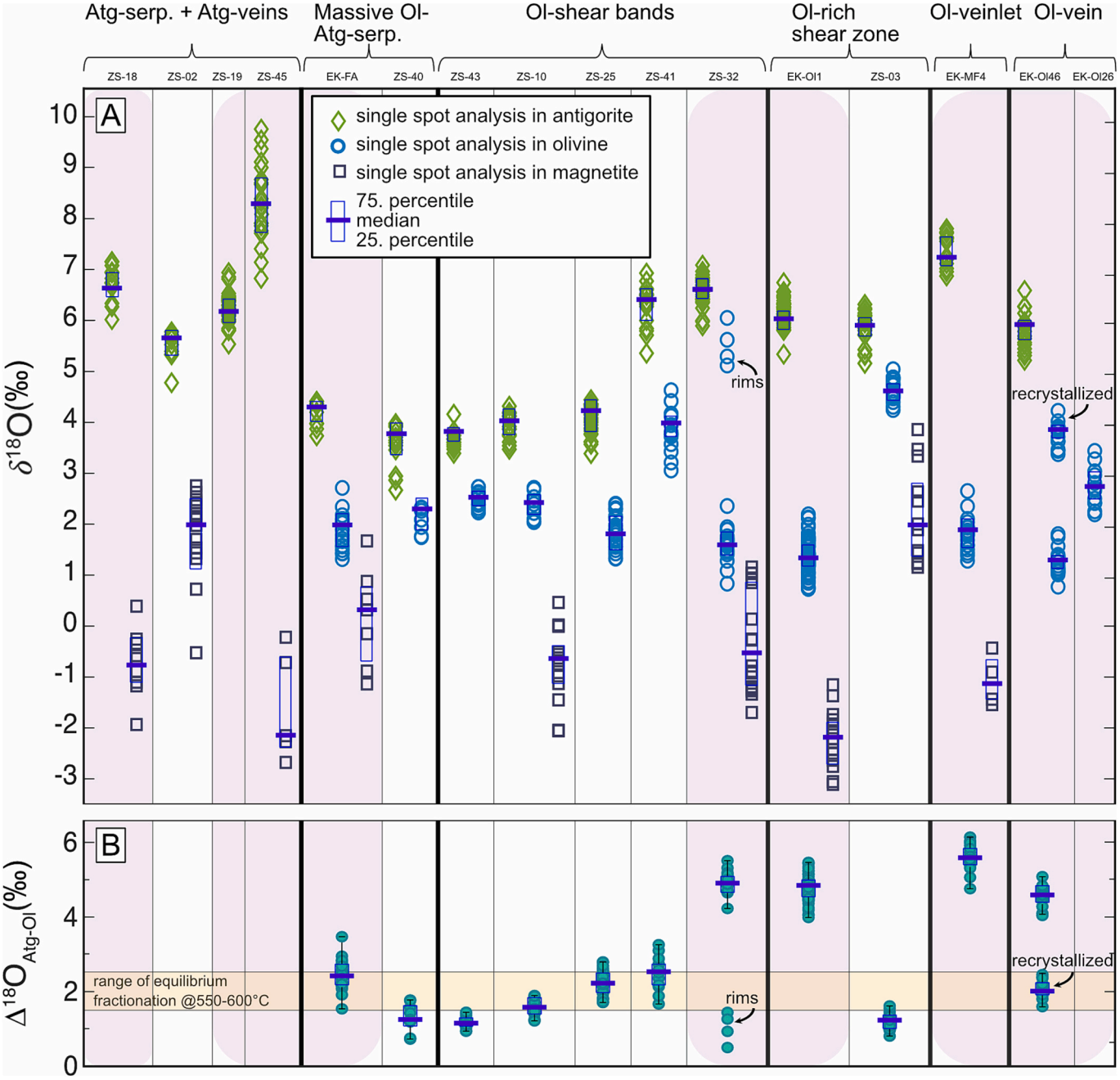

Fig. 9. Summary of the oxygen isotope results. A) $\delta^{18}O$ values of antigorite, olivine, and magnetite (in ‰ relative to V-SMOW) of different samples arranged in order of olivine texture. Colored symbols are single-spot analyses, while boxes show the 25th and 75th percentiles with the median value per sample. The purple vertical bands in the background of the data represent samples from LTG, while samples from UTG are plotted on a white background. B) Calculated fractionation between antigorite and olivine in the different samples. The orange horizontal band illustrates the equilibrium fractionation between antigorite and olivine, with $\Delta^{18}O_{Atg\text{-}Ol} \sim +1.5$–$2.5$ ‰. This is fulfilled for all UTG samples, but only for the sample EK-FA with olivine grown in massive Ol-Atg-serpentinite, and for recrystallized late olivine (samples ZS-32 and EK-Ol46) from LTG. (For interpretation of the references to colour in this figure legend, the reader is referred to the web version of this article.)

serpentinites lose most of these elements, especially U, Cl, Br, I, Sr, Li and B. Therefore, subducted serpentinites are depleted in these elements compared to abyssal serpentinites (e.g., Deschamps et al., 2013; Scambelluri et al., 2004a; Pettke and Bretscher, 2022; Scambelluri and Tonarini, 2012). However, Pagé and Hattori (2017) showed that some fluid mobile elements, such as F and B, are preferentially retained over Cl, Br and I.

Within the Zermatt-Saas serpentinites, antigorite shows a strong enrichment of As, Sb and B (Fig. 6A), while Cl is only slightly enriched compared to the primitive mantle (Clarke et al., 2020; antigorite 6–31 µg/g Cl, corresponding to an enrichment factor of ~0.4–1.8). Boron shows enrichment factors of mostly 30–40 but up to 90 with B contents ranging between 4 and 28 µg/g (Fig. 7A). Even higher enrichment factors of up to 470 and 580 are observed for As and Sb, respectively. Arsenic and Sb concentrations in antigorite are higher in LTG samples than UTG samples (Fig. 7B). Assuming a preserved oceanic imprint, this difference suggests different serpentinization settings with different proximity to the seafloor, with a typical increase in As and Sb closer to the seafloor (Pettke and Bretscher, 2022; Andreani et al., 2014), corresponding to the LTG site.

Varying proximity to the seafloor may imply different serpentinization temperatures, with generally higher temperatures at depth (e.g.,

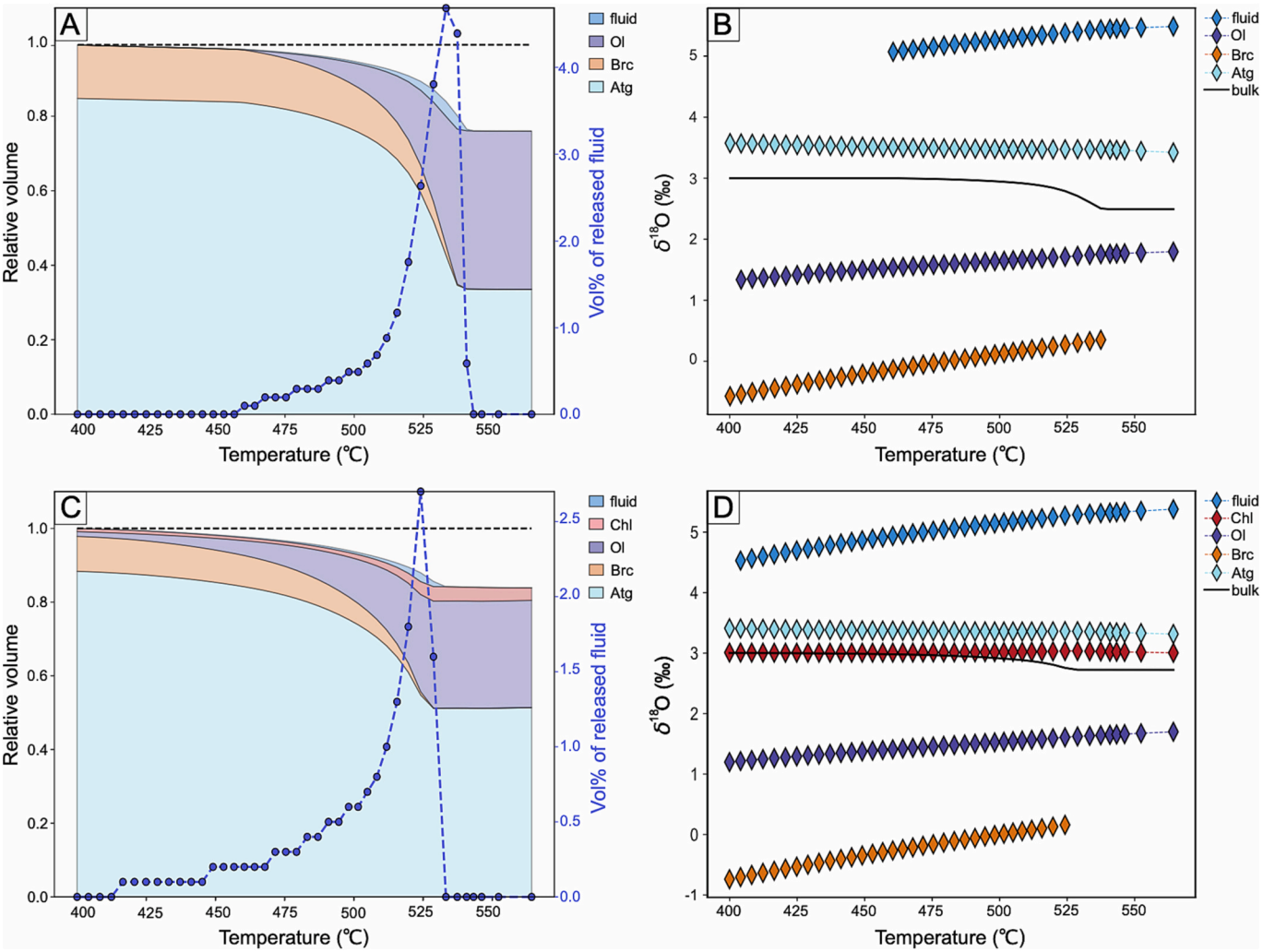

Fig. 10. Results of thermodynamic and oxygen isotope fractionation modeling, using the bulk composition of Rock 1 with 41.25 wt% SiO_2, 0.88 wt% Al_2O_3, 2.98 wt % FeO, and 47.27 wt% MgO, and Rock 2 with 40.0 wt% SiO_2, 2.2 wt% Al_2O_3, 4.4 wt% FeO, and 42.0 wt% MgO. The components TiO_2, Fe_2O_3, MnO, CaO, Na_2O and K_2O are set to 0.0 wt% A) Predicted stable mineral assemblage and modeled fluid release based on fluid production for Rock1. B) Calculated $\delta^{18}O$ values of stable phases in ‰ relative to V-SMOW at different temperatures for Rock 1. C) Predicted stable mineral assemblage and modeled fluid release based on fluid production for Rock 2. D) Calculated $\delta^{18}O$ values of stable phases in ‰ relative to V-SMOW at different temperatures for Rock 2.

Agrinier and Cannat, 1997). The B content in serpentine has been shown to be inversely correlated with temperature (e.g., Bonatti et al., 1984; Thompson and Melson, 1970; Seyfried and Dibble, 1980). This may explain the positive As(—Sb)-B correlation within each of the two outcrop parts (Fig. 7A). While the As and Sb concentration in antigorite is higher in LTG samples, the B content in antigorite is comparable between LTG and UTG samples. This may raise the question of a different fluid/rock ratio and a different fluid chemistry during serpentinization for the two outcrop parts. Fluid/rock ratio and fluid chemistry controlling B uptake in serpentinites has been suggested by Plas (1997) and Boschi et al. (2008) where no correlation between B content and O-isotope temperature was observed.

Beside As, Sb and B variability, also a significant variability in $\delta^{18}O$ is observed in the antigorite among the samples studied. LTG samples generally contain antigorite with the higher $\delta^{18}O$ values and, with exception of the Atg-vein of sample ZS-45, are fairly homogenous with average values of +6 to +7 ‰. Antigorite from UTG samples is more heterogeneous with four samples having $\delta^{18}O$ values of ~ +4 ‰ and three samples having $\delta^{18}O$ values of +6 to +7 ‰. The $\delta^{18}O$ of antigorite measured in this study is in the same range as the bulk $\delta^{18}O$ of HP serpentinites from other localities of the Zermatt-Saas unit. For example, antigorite separates have $\delta^{18}O$ values of +3 to +4 ‰ at Pfulwepass (Widmer, 1996), +4 to +5 ‰ at Trockener Steg (Seydoux and Baumgartner, 2013) and + 5 to +6 ‰ in Mellichen near Täsch (Cartwright and Barnicoat, 1999). In Valtournache, the Zermatt-Saas serpentinites have even lower bulk $\delta^{18}O$ values of +1 to +3 ‰ (Cartwright and Barnicoat, 1999), and antigorite has $\delta^{18}O$ values of +1 to +6 ‰ (Rubatto et al., 2023).

Serpentinization temperatures can be calculated assuming that the $\delta^{18}O$ of antigorite is inherited from the oceanic lizardite. Using the fractionation factors from the experimental study of Saccocia et al. (2009), and assuming seawater with $\delta^{18}O$ of 0 ‰, the high $\delta^{18}O_{Atg}$ of +6 to +7 ‰ would indicate oceanic serpentinization at lower temperatures of ~180–210 °C, and samples with $\delta^{18}O_{Atg}$ of ~ +4 ‰ were serpentinized at higher temperatures of ~230–250 °C.

In our study, B and As contents of antigorite are positively correlated with antigorite $\delta^{18}O$ in each outcrop part (S5). This correlation suggests that temperature was the dominant factor controlling B and $\delta^{18}O$ variability in antigorite within each outcrop part. Additionally, also a different fluid/rock ratio might have played a role over the studied area.

With LTG samples having higher $\delta^{18}O_{Atg}$ values and higher As and Sb concentrations than UTG samples (S5), we propose that the ultramafic rocks from the LTG site were serpentinized at lower temperature, probably in a setting closer to the seafloor than the rocks from the UTG

site.

Alternatively, it has been proposed that enrichments in As and Sb may be the result of contamination by sediment-derived fluids at the lizardite–antigorite transition during early subduction (Deschamps et al., 2011; Lafay et al., 2013; Cannaò et al., 2016). Interaction with metasedimentary fluids could also account for higher $\delta^{18}O$ in serpentinites (e.g., Cartwright and Barnicoat, 1999; Barnes et al., 2014; Vho et al., 2020). However, in our samples, As and Sb are also enriched in samples with low $\delta^{18}O$ of ~ +4 ‰ in antigorite (sample EK-FA). Furthermore, the enrichment is As and Sb is not associated with increases in Ba, Rb and Pb reported in Alpine serpentinites due to infiltration of sediment-derived fluids (e.g., Barnes et al., 2014). These features are not consistent with an input of sediment-derived fluids in the studied Zermatt-Saas samples. This conclusion is consistent with the study of Gilio et al. (2019). They concluded, based on fluid-mobile element compositions coupled with Sr and Pb isotopic compositions, that the Zermatt-Saas serpentinites had only limited interactions with slab-derived subduction fluids during subduction and rather behaved as a closed system, retaining an oceanic geochemical signature.

6.2. Homogenization during lizardite-antigorite transition

Oceanic serpentinization produces lizardite and chrysotile, as also reported for the Atlantis Massif, which may provide a similar serpentinization setting to the Zermatt-Saas ophiolite (e.g., Früh-Green et al., 2004). Bulk $\delta^{18}O$ values of serpentine separates from the Atlantis Massif range from +2.7 to +5.5 ‰ (Früh-Green et al., 2004). A recent study from Rouméjon et al. (2018) reported within sample variability in $\delta^{18}O$ of up to ~4 ‰ in lizardite from the Atlantis Massif and up to ~5 ‰ in lizardite from the Southwest Indian Ridge. In samples from passive margin serpentinites (Galicia and Newfoundland Margin), lizardite varies in $\delta^{18}O$ within sample by up to 12 ‰ depending on textural domains (Vesin et al., 2023).

Compared to the variability of lizardite from oceanic serpentine, the $\delta^{18}O$ range of antigorite in the Zermatt-Saas samples is more restricted: the within-sample variability is generally <2 ‰ (Fig. 9). Therefore, we suggest that the transformation of lizardite and chrysotile to antigorite during prograde metamorphism generally homogenizes the oxygen isotopic composition at the microscale.

After the transformation of lizardite and chrysotile into antigorite at 300–350 °C (Evans, 2004; Schwartz et al., 2013), antigorite remained stable, and its oxygen isotopic composition is internally adjusted with increasing temperature. Evidence for this re-equilibration is observed in samples ZS-03 or ZS-25, where antigorite shows a significant Al zonation (Fig. 5B), which is attributed to growth at different temperature (e.g., Padrón-Navarta et al., 2013; Kempf et al., 2020). SIMS analysis yields the same $\delta^{18}O$ within uncertainty for both zones, suggesting antigorite recrystallization in a closed system for oxygen isotopes. There is no major metamorphic reaction between ~350 and ~ 500 °C that would change the assemblage of the serpentinite (Kempf et al., 2020) and thus the internal adjustment of the $\delta^{18}O$ composition was only minimal if the rocks remained closed for external fluids. The temperature calculations from antigorite $\delta^{18}O$ presented in Section 6.1 thus assume that the precursor lizardite or chrysotile had the same bulk $\delta^{18}O$ as antigorite, although possibly in a less restricted range.

6.3. Olivine formation during subduction by different processes

6.3.1. In-situ olivine formation by dehydration reaction

Olivine grown as pervasive replacement in dispersed patches or in the "zebra-like" domains in massive Ol-Atg-serpentinite are considered to represent olivine produced in situ via the antigorite+brucite dehydration reaction (eq. 1a, Evans and Trommsdorff, 1970):

$$\mathrm{Atg} + \mathrm{Brc} = \mathrm{Ol} \pm \mathrm{Chl} + \mathrm{H_2O} \quad (1a)$$

The occurrence of olivine is attributed to the former distribution of brucite-rich domains (Kempf et al., 2020). The two samples (EK-FA and ZS-40) that show such replacement olivine (Ol1) have average $\Delta^{18}O_{Atg\text{-}Ol}$ of +2.4 ± 1.1 ‰ and +1.3 ± 1.2 ‰, respectively (Table 1 and Fig. 9B). These values are within the expected range for equilibrium fractionation: $\Delta^{18}O_{Atg\text{-}Ol}$ of +1.5–2.5 ‰ at 550–600 °C, according to the fractionation factor compilation of Vho et al. (2019), which includes the studies from e.g., Zheng (1993a and 1993b). Therefore, we propose isotopic equilibrium between the educt phase antigorite and the product phase olivine.

In addition to the replacement Ol1 crystals, in both samples there are cross cutting olivine bands consisting of polygonal olivine (Ol2) and representing the first fluid channelization (Fig. 4A). Ol2 in the bands has $\delta^{18}O$ of +1 to +2 ‰ and is isotopically similar to Ol1, but Ol2 polygons are more Fe-rich than Ol1 (sample EK-FA, Fig. 5C). This suggests that Ol1 and Ol2 likely represent two distinct stages of olivine crystallization with the same $\delta^{18}O$. We propose that the formation of Ol2 in equilibrium with Ol1 and antigorite is due to locally sourced fluids, released during Ol1 formation.

The measured olivine with $\delta^{18}O$ of +1 to +2 ‰ and antigorite with $\delta^{18}O$ of +3 to +4 ‰ match the modeled $\delta^{18}O$ values (Fig. 10B and D). This further confirms that antigorite and olivine are in isotopic equilibrium. As the modeling shows, $\Delta^{18}O_{Atg\text{-}Ol}$ of +1.5–2.5 ‰ can be reached over a temperature range, and Ol2 might also have formed at slightly different temperatures than Ol1.

Vieira Duarte et al. (2021) suggested that magnetite (Mt_2) is formed along the dehydration reaction of brucite + antigorite (eq. 1b), by adapting the former reaction from Evans and Trommsdorff (1970):

$$\mathrm{Atg} + \mathrm{Brc} + \mathrm{Mt_1} = \mathrm{Ol} \pm \mathrm{Chl} + \mathrm{Mt_2} + \mathrm{H_2O} \quad (1b)$$

where Mt_1 is magnetite formed during oceanic serpentinization. In the samples studied, the magnetite mesh texture is enclosed by Ol1, but is absent in the polygonal Ol2. Ol2 is Fe-richer due to Mg—Fe exchange between reacting magnetite and olivine (Kempf et al., 2020; and Fig. 5C). The $\Delta^{18}O_{Ol\text{-}Mt}$ is about +3 ‰ for temperatures of 550–600 °C, using fractionation factors from Vho et al. (2019). Magnetite in sample EK-FA shows a $\Delta^{18}O_{Ol\text{-}Mt}$ of +1.7 ± 2.2 ‰ with coexisting olivine (Table 1) and this indicates isotopic equilibrium with olivine and antigorite at the conditions of the dehydration reaction.

6.3.2. Isotopic equilibrium vs. disequilibrium due to reactive fluid flow

Several samples, including Ol-shear bands, Ol-shear zones and Ol-veins, display isotopic disequilibrium between olivine and antigorite (Fig. 9B), suggesting different olivine-forming processes or conditions. This is supported by the high amount of olivine concentrated in shear bands, shear zones and veins (locally up to >90 vol%), indicating a process that can enrich olivine relative to in-situ produced olivine. A mechanism for the formation of Ol-veins and Ol-networks by reactive fluid flow has been proposed for the Ol-bearing HP serpentinites from the Erro-Tobbio Massif in northwestern Italy (Plümper et al., 2017; Huber et al., 2022). Huber et al. (2022) explored the formation of nearly pure Ol-veins using thermodynamic equilibrium calculations and numerical modeling. In their model, they suggest that fluid released by the dehydration reaction from brucite-rich portions of the rock, called source regions, carries a very low Si potential and can trigger further isothermal dehydration by antigorite breakdown in domains adjacent to the source regions to form olivine without the involvement of brucite. The resulting olivine is formed due to reactive fluid flow and concentrates where the fluid passes, leading to vein widening and olivine purification. However, the model by Huber et al. (2022) only considers a simplified fluid, and neglects solute transport (e.g., Mg), which had been shown to play an important role in deep earth fluids by other studies (e.g., Huang and Sverjensky, 2019; Tiraboschi et al., 2017). The reaction of antigorite with a fluid enriched in Mg-species represents another potential mechanism to form olivine in shear bands and veins by reactive fluid flow. Jabaloy-Sánchez et al. (2022) consider the Mg-rich aqueous fluids to be responsible for nearly monomineralic Ol-veins that formed

synkinematically with the brucite-out reaction in HP serpentinites from the Cerro del Almirez Massif in southern Spain, and they are comparable to the Ol-shear bands and Ol-rich shear zones from this study (e.g., Fig. 2B and C).

Olivine formed by reactive fluid flow may lead to either isotopic equilibrium or disequilibrium with antigorite, depending on whether the fluid involved is sourced locally or externally from serpentinite domains with a different isotopic composition. Indeed, both cases of i) isotopic equilibrium and ii) isotopic disequilibrium are observed among the polygonal olivine (Ol2) in Ol-shear bands and Ol-rich shear zones.

i) Isotopic equilibrium is found within all Ol-shear bands and Ol-rich shear zones of UTG, where we observe samples with $\Delta^{18}O_{Atg\text{-}Ol}$ of ~ +1.5–2.5 ‰ (Fig. 9B), regardless of high or low $\delta^{18}O_{Atg}$ (Fig. 9A). Magnetite in textural equilibrium with the polygonal olivine, also displays isotopic equilibrium. Isotopic equilibrium between olivine, antigorite, and magnetite implies that the fluid responsible for this process was in equilibrium with the antigorite and was likely locally sourced. Local equilibrium between olivine and antigorite has already been proposed for the UTG area based on in-situ boron isotopes (Clarke et al., 2020). Locally sourced fluids for this part of the outcrop are also consistent with the study by Bouilhol et al. (2022), where they used C, O, and Sr isotopes to show that carbonate-bearing olivine-diopside veins at Trockener Steg were formed by fluids derived from the serpentinites. The $\delta^{18}O$ of vein olivine by Bouilhol et al. (2022) ranges from +3.1 to +5.7 ‰ and is in the same range as the olivine from Ol-shear bands (ZS-41 + 3.8 ± 0.9 ‰) and the Ol-rich shear zone (ZS-03 + 4.6 ± 0.5 ‰) from our study.

ii) Isotopic disequilibrium between olivine and antigorite is observed in all sampled Ol-shear bands, Ol-rich shear zones and Ol-veins from LTG with $\Delta^{18}O_{Atg\text{-}Ol}$ of +4–6 ‰ (Fig. 9B). The olivine in these samples has low $\delta^{18}O$ of +1 to +2 ‰, while the antigorite always displays high $\delta^{18}O$ of +6 to +7 ‰ (Fig. 9A). The isotopic disequilibrium suggests that an externally sourced fluid was involved (see details in Section 6.4; Fig. 11, case C). However, the magnetite O isotope composition indicates equilibrium with the polygonal olivine in the shear bands and shear zones. Therefore, it is proposed that magnetite forms/recrystallizes alongside the olivine during reactive fluid flow.

The high $\Delta^{18}O_{Atg\text{-}Ol}$ of +4–6 ‰ in the case ii) samples (Fig. 9B) cannot represent isotopic equilibrium between antigorite and olivine by destabilization of lizardite, as temperatures as low as 150–300 °C would be required to obtain such a high fractionation. Furthermore, low temperature isotopic equilibration is also negated by the high olivine Mg# of 94–96, which requires a minimum reaction temperature of about 550 °C for the bulk compositions of the Zermatt-Saas samples (Kempf et al., 2020). Therefore, we conclude that the majority of olivine formed at the relatively narrow high P-T conditions of 2.2–2.5 GPa and 550–600°C. However, some retrograde features are present throughout the studied area, e.g., late greenschist-facies tremolite-actinolite-talc-carbonate veins with serpentine halos (Kempf et al., 2020), and calcite likely retrogressed from aragonite (e.g., sample EK-Ol46 and ZS-03). Antigorite with high $\delta^{18}O$ resulting from recrystallization by fluids from late tremolite-actinolite-talc-carbonate veins at the LTG outcrop is rather unlikely as there is no difference in elemental systematics between antigorite with high $\delta^{18}O$ and antigorite with low $\delta^{18}O$ from EK-

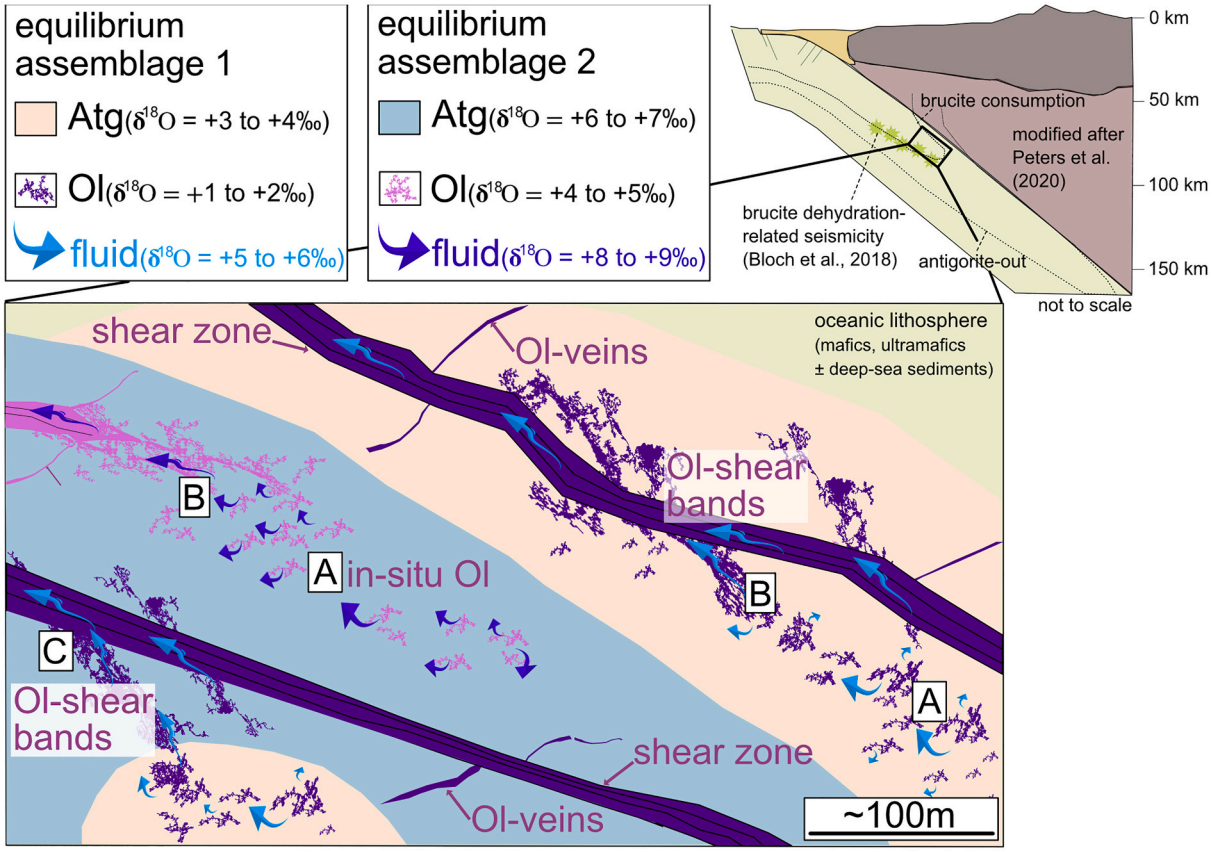

Fig. 11. Conceptualized fluid model showing internal versus external fluids leading to isotopic dis/equilibrium. Case A: Olivine and fluid are produced in situ in brucite-rich portions of the Atg-serpentinite, leading to isotopic equilibrium between olivine and antigorite. Case B: Olivine in shear bands and shear zones are formed by an internally sourced fluid and olivine is therefore in isotopic equilibrium with antigorite. Case C: Olivine in shear bands and shear zones (and veins) is formed by an externally sourced fluid from a serpentinite domain with a different isotopic composition and olivine is therefore in isotopic disequilibrium with antigorite.

FA (see S6 for location of samples and the late veins). Only the minor olivine recrystallized at rims of Ol2 polygons or along cracks in samples ZS-32 and EK-Ol46 (Fig. 5E and F) may represent a minor stage of later recrystallization. The recrystallized olivine has higher Mg# and $\delta^{18}O$ than the main olivine and is isotopically in equilibrium with the surrounding antigorite (Fig. 9B), indicating local re-equilibration after the infiltrating fluid has passed through the rock.

6.3.3. Elemental systematics of olivine

The trace element composition of antigorite is mainly controlled by the serpentinization setting and the element loss during prograde subduction (Section 6.1). Elemental systematics of olivine are affected by dehydration reactions and subsequent fluid flow, leading to different behavior for fluid-immobile and fluid-mobile elements. Fluid-immobile elements in olivine are not strongly affected by dehydration reactions and subsequent fluid flow. This is indicated by elements such as Ni, Co, and Zn. These elements show the same antigorite/olivine partitioning for olivine produced in situ by pervasive replacement and for olivine formed by reactive fluid flow in Ol-shear zones and Ol-veins (S5).

Element redistribution during dehydration reactions is important especially for fluid-mobile elements (e.g., Scambelluri et al., 2019; Pettke and Bretscher, 2022). The olivine analyzed in this study is highly enriched in B and As compared to the primitive mantle. The overall higher As and Sb concentrations in olivine from LTG compared to olivine from UTG are likely not controlled by fluid flow, but by oceanic As and Sb enrichments in the serpentinites in this part of the outcrop (Fig. 7B). Olivine in LTG samples is also enriched in Sb. Such enrichment in fluid-mobile trace elements, especially for B, has been also reported for metamorphic olivine in other localities (e.g., De Hoog et al., 2014; Tenthorey and Hermann, 2004). The high concentrations of B, As and Sb in the Zermatt-Saas metamorphic olivine suggest that these fluid-mobile elements can be incorporated into the newly formed olivine in high concentrations. At UTG, olivine shows increasing As and B concentrations with its prograde textural evolution, from olivine formed in-situ to olivine formed in shear bands and shear zones, associated to increasing fluid fluxes. At LTG, only enrichment in As with prograde textural evolution is observed, while B concentration in olivine remains constant (Fig. 8A). We hypothesize that this may be due to limited B incorporation into olivine due to differences in fluid pH.

Boron enrichment in olivine, mainly in zones of high fluid flux such as shear zones and veins, and generally in the more deformed outcrop part of UTG, results in higher [B]Ol/[B]Atg values compared to [B]Ol/[B]Atg in massive Ol-Atg-serpentinites and Ol-veinlets (Fig. 8B and C). [B]Ol/[B]Atg has also been suggested to serve as a proxy for internal versus external fluids (e.g., Scambelluri et al., 2019; Clarke et al., 2020). Of the samples studied that show oxygen isotope equilibrium, only one sample falls within the [B]Ol/[B]Atg equilibrium range suggested by Clarke et al. (2020) (Fig. 8C). Moreover, samples equilibrated in oxygen isotopes vary in their [B]Ol/[B]Atg values from 0.5 to 3.1. We consider oxygen isotope equilibrium to be a more robust proxy for internal versus external fluids because it is based on a major element whose systematic is better understood. The B partitioning between olivine and antigorite may instead be indicative of the amount of fluid flux and possibly fluid pH, rather than being a proxy for internal versus external fluids.

6.4. Isotopic composition of released fluids and fluid pathways

Based on textures and olivine abundance within the continuous body of HP serpentinites of this study, there are two different types of olivine formation: i) antigorite+brucite dehydration reaction in parts where brucite was present, representing sites of fluid and olivine production, and ii) olivine in Ol-shear bands, Ol-shear zones and Ol-veins, representing fluid transfer sites where a Mg-rich, Si-poor fluid reacts with antigorite to crystallize olivine. This represents a change from a porous flow at the production site of the fluid to a channelized flow for the fluid transfer. Channelization of the fluid flow is expected because the replacement of antigorite by olivine during the dehydration reaction leads to a reduction in volume and thus changes the porosity and the fluid pressure at the microscale (Plümper et al., 2017). This process increases permeability, which is otherwise relatively low in serpentinites (10^{-24} m^2–$10^{-20.5}$$m^2$, Kawano et al., 2011, Ganzhorn et al., 2019, 10^{-15} m^2, Eberhard et al., 2022). This increase in porosity and permeability allows the fluids to be expelled, producing olivine during reactive fluid transport, leading to positive feedback for fluid channeling (Plümper et al., 2017). Fluid channels are represented by shear bands and shear zones because they represent zones of stronger deformation, and permeability can reach one to two orders of magnitude higher due to the increase in porosity with deformation (Ganzhorn et al., 2019).

The fluid channels or pathways can be traced because the affected serpentinites have different trace elements and oxygen isotopic composition. The oxygen isotopic composition of the equilibrated serpentinite samples helps to constrain the isotopic composition of the fluids released. Because the fluids and olivine are produced simultaneously during the dehydration reaction, equilibrium fractionation between olivine and fluid is expected ($\Delta^{18}O_{fluid\text{-}Ol}$ at 550–600 °C is ~ +4 ‰; Vho et al., 2019 and references therein; Fig. 10B and D). Equilibrated samples fall into two groups with $\delta^{18}O_{Ol}$ of +1 to +2 ‰ and $\delta^{18}O_{Ol}$ of +4 to +5 ‰, resulting in fluids with $\delta^{18}O$ of +5 to +6 ‰ and $\delta^{18}O$ of +8 to +9 ‰ (Fig. 11, case A). The migration and interaction of these fluids with serpentinite rocks that have the same isotopic composition as the source rock crystallizes olivine in isotopic equilibrium (Fig. 11, case B). When fluids with $\delta^{18}O$ +5 to +6 ‰ infiltrate Atg-serpentinites of different isotopic composition ($\delta^{18}O$ + 6 to +7 ‰), the crystallized olivine will have $\delta^{18}O$ of +1 to +2 ‰ and be in isotopic disequilibrium with the surrounding antigorite (e.g., LTG samples ZS-32, EK-Ol1 and EK-Ol46) (Fig. 11, case C). Fluids derived from dehydrating metasediments or altered oceanic crust (mainly due to lawsonite, amphibole or chlorite destabilization at 500–560 °C and 2.1–2.2 GPa) generally have a higher $\delta^{18}O$ of +15 to +25 ‰ and + 7 to +10 ‰, respectively (e.g., Vho et al., 2020) and cannot account for the formation of olivine with low $\delta^{18}O$ in isotopic disequilibrium with antigorite.

In our study, the oxygen isotope disequilibrium, which is restricted to samples collected from Ol-shear bands, Ol-rich shear zones and Ol-veins, is the key to detecting the influx of an external fluid into the rock volume of serpentinites and documents channelized fluids at the 100 m to km scale.

7. Conclusions

Based on the acquired dataset of in-situ oxygen isotopes and trace elements in antigorite, metamorphic olivine and magnetite from HP serpentinites, the following main conclusions are drawn:

(1) The Zermatt-Saas serpentinites in the study area record variable serpentinization conditions. The two parts of the outcrop record different temperatures and proximities to the seafloor during the hydration of the ultramafic rocks in the Piedmont-Ligurian oceanic lithosphere.
(2) The oxygen isotopic composition of antigorite in subducted serpentinites is relatively homogeneous at the sample scale compared to that of serpentine (lizardite) from abyssal serpentinites, suggesting sample-scale homogenization during the prograde transition from lizardite to antigorite. The geochemical results are not consistent with infiltration of sedimentary fluids at any stage of this process.
(3) The trace element and oxygen isotope compositions of antigorite are mainly controlled by the serpentinization conditions and the early subduction history. In contrast, the equilibrium and disequilibrium between antigorite and olivine are determined by the brucite dehydration reaction and the structurally controlled fluid flow during the Alpine subduction history.

(4) Brucite + antigorite dehydration produced metamorphic olivine and aqueous fluid in isotopic equilibrium, represented by olivine grown in pervasive replacement patterns within the HP serpentinite.
(5) As porosity increased with the dehydration reaction, fluid was expelled, and olivine was produced in shear bands, shear zones and veins via reactive fluid flow. Such olivine can be either in isotopic equilibrium or in disequilibrium with antigorite, depending on whether the fluid was internal or external. The presence of the non-equilibrated olivine in Ol-shear bands and nearly pure Ol-veins at LTG demonstrates channelized fluid flow in subduction zone settings and shows that oxygen isotope disequilibrium can be used to trace fluid infiltration.
(6) Metamorphic olivine with $\delta^{18}O$ values of ~ +1 to +2 ‰ and ~ +4 to +5 ‰ corresponds to a released fluid of ~ +5 to +6 ‰ and ~ +8 to +9 ‰, respectively. This study demonstrates that fluids released from subducted serpentinites can have variable $\delta^{18}O$ under forearc conditions and are related to the isotopic variability of the serpentinites acquired during seafloor alteration.

CRediT authorship contribution statement

Michelle Ulrich: Conceptualization, Data curation, Formal analysis, Investigation, Methodology, Visualization, Writing – original draft. **Daniela Rubatto:** Funding acquisition, Project administration, Supervision, Validation, Writing – review & editing, Resources, Conceptualization. **Jörg Hermann:** Supervision, Validation, Writing – review & editing, Conceptualization. **Thorsten A. Markmann:** Software, Visualization, Writing – review & editing. **Anne-Sophie Bouvier:** Methodology, Writing – review & editing. **Etienne Deloule:** Methodology, Writing – review & editing.

Declaration of competing interest

The authors declare that they have no known competing financial interests or personal relationships that could have appeared to influence the work reported in this paper.

Data availability

All data can be found in the manuscript and in the supplementary materials.

Acknowledgments

We thank Elias Kempf for explaining the field area, providing samples and for his help during sample collection, together with Francesca Piccoli and Coralie Vesin. Francesca Piccoli and Renée Tamblyn are acknowledged for assistance during the LA-ICP-MS analyses, Coralie Vesin, Hugo Dominguez, and Pierre Lanari for assistance during EPMA analyses, Alfons Berger for introduction to the SEM facility. The team of the SwissSIMS (University of Lausanne) and CRPG-CNRS (University of Lorraine, Nancy) are thanked for their support during the analytical session. Thomas Aebi, Nadine Lötscher and Stephan Brechbühl are acknowledged for preparing the thin sections and polishing the SIMS reference materials. This manuscript benefited from fruitful discussions with Elias Kempf, Francesca Piccoli, Thomas Pettke, Konstantin Huber, Lisa Eberhard, José-Alberto Padrón-Navarta, and Guillaume Siron. DR acknowledges the financial support of the Swiss National Science Foundation (SNSF 200021_19959). We thank Enrico Cannaò and one anonymous reviewer for insightful and constructive comments, and Sonja Aulbach for efficient editorial handling.

Appendix A. Supplementary data

Supplementary data to this article can be found online at https://doi.org/10.1016/j.chemgeo.2024.121978.

References

Agard, P., Yamato, P., Jolivet, L., Burov, E., 2009. Exhumation of oceanic blueschists and eclogites in subduction zones: timing and mechanisms. Earth Sci. Rev. 92 (1), 53–79. https://doi.org/10.1016/j.earscirev.2008.11.002.
Agrinier, P., Cannat, M., 1997. Oxygen-isotope constraints on serpentinization processes in ultramafic rocks from the mid-Atlantic ridge (23°N). Proc. Ocean Drill. Program Sci. Results 153, 381–388.
Ague, J.J., 2014. Fluid flow in the deep crust. In: Rudnick, R. (Ed.), The Crust, vol. 4. Elsevier, Amsterdam, pp. 203–247.
Alt, J.C., Garrido, C.J., Shanks, W.C., Turchyn, A., Padrón-Navarta, J.A., López Sánchez-Vizcaíno, V., Marchesi, C., 2012. Recycling of water, carbon, and sulfur during subduction of serpentinites: a stable isotope study of Cerro del Almirez, Spain. Earth Planet. Sci. Lett. 327–328, 50–60. https://doi.org/10.1016/j.epsl.2012.01.029.
Andreani, M., Escartin, J., Delacour, A., Ildefonse, B., Godard, M., Dyment, J., Fallick, A. E., Fouquet, Y., 2014. Tectonic structure, lithology, and hydrothermal signature of the Rainbow massif (Mid-Atlantic Ridge 36°14′ N). Geochem. Geophys. Geosyst. 15, 3543–3571. https://doi.org/10.1002/2014GC005269.
Angiboust, S., Agard, P., Jolivet, L., Beyssac, O., 2009. The Zermatt-Saas ophiolite: the largest (60-km wide) and deepest (c. 70-80 km) continuous slice of oceanic lithosphere detached from a subduction zone. Terra Nova 21 (3), 171–180. https://doi.org/10.1111/j.1365-3121.2009.00870.x.
Barnes, J.D., Beltrando, M., Lee, C.-T.A., Cisneros, M., Loewy, S., Chin, E., 2014. Geochemistry of Alpine serpentinites from rifting to subduction: a view across paleogeographic domains and metamorphic grade. Chem. Geol. 389, 29–47. https://doi.org/10.1016/j.chemgeo.2014.09.012.
Bearth, P., 1967. Die Ophiolite der Zone von Zermatt-Saas Fee. Beiträge zur geologischen Karte der Schweiz N.F 132, 130.
Bearth, P., 1974. Zur Gliederung und Metamorphose der Ophiolite der Westalpen. Schweiz. Mineral. Petrogr. Mitt. 54, 385–396.
Bebout, G.E., 1995. The impact of subduction-zone metamorphism on mantle-ocean chemical cycling. Chem. Geol. 126 (2), 191–218.
Bloch, W., John, T., Kummerow, J., Salazar, P., Krüger, O.S., Shapiro, S.A., 2018. Watching dehydration: seismic indication for transient fluid pathways in the oceanic mantle of the subducting Nazca Slab. Geochem. Geophys. Geosyst. 19 (9), 3189–3207.
Bonatti, E., Lawrence, J.R., Morandi, N., 1984. Serpentinization of ocean-floor peridotites: temperature dependence on mineralogy and boron content. Earth Planet. Sci. Lett. 70, 88–94. https://doi.org/10.1016/0012-821X(84)90211-5.
Boschi, C., Dini, A., Früh-Green, G.L., 2008. Isotopic and element exchange during serpentinization and metasomatism at the Atlantis Massif (MAR 30 degrees N): insights from B and Sr isotope data. Geochim. Cosmochim. Acta 72, 1801–1823. https://doi.org/10.1016/j.gca.2008.01.013.
Bouilhol, P., Debret, B., Inglis, E.C., Warembourg, M., Grocolas, T., Rigaudier, T., Villeneuve, J., Burton, K.W., 2022. Decoupling of inorganic and organic carbon during slab mantle devolatilization. Nat. Commun. https://doi.org/10.1038/s41467-022-27970-0.
Bovay, T., Rubatto, D., Lanari, P., 2021. Pervasive fluid-rock interaction in subducted oceanic crust revealed by oxygen isotope zoning in garnet. Contrib. Mineral. Petrol. 176 (55) https://doi.org/10.1007/s00410-021-01806-4.
Bucher, K., Grapes, R., 2009. The eclogite-facies Allalin Gabbro of the Zermatt-Saas ophiolite, Western Alps: a record of subduction zone hydration. J. Petrol. 50 (8), 1405–1442. https://doi.org/10.1093/petrology/egp035.
Bucher, K., Fazis, Y., De Capitani, C., Grapes, R., 2005. Blueschists, eclogites, and decompression assemblages of the Zermatt-Saas ophiolite: high-pressure metamorphism of subducted Tethys lithosphere. Am. Mineral. 90 (5–6), 821–835. https://doi.org/10.2138/am.2005.1718.
Bucher, K., Weisenberger, T.B., Weber, S., Klemm, O., Corfu, F., 2020. The Theodul Glacier Unit, a slab of pre-Alpine rocks in the Alpine meta-ophiolite of Zermatt-Saas, Western Alps. Swiss J. Geosci. 113, 1. https://doi.org/10.1186/s00015-020-00354-6.
Cannaò, E., Scambelluri, M., Agostini, S., Tonarini, S., Godard, M., 2016. Linking serpentinite geochemistry with tectonic evolution at the subduction plate-interface: the Voltri Massif case study (Ligurian Western Alps, Italy). Geochim. Cosmochim. Acta 190, 115–133. https://doi.org/10.1016/j.gca.2016.06.034.
Cartwright, I., Barnicoat, A.C., 1999. Stable isotope geochemistry of Alpine ophiolites: a window to ocean-floor hydrothermal alteration and constraints on fluid–rock interaction during high-pressure metamorphism. Int. J. Earth Sci. 88 (2), 219–235. https://doi.org/10.1007/s005310050261.
Cartwright, I., Barnicoat, A., 2002. Petrology, geochronology, and tectonics of shear zones in the Zermatt-Saas and Combin zones of the Western Alps. J. Metamorph. Geol. 20 (2), 263–281. https://doi.org/10.1046/j.0263-4929.2001.00366.x.
Clarke, E., De Hood, J.C.M., Kirstein, L.A., Harvey, J., Debret, B., 2020. Metamorphic olivine records external fluid infiltration during serpentinite dehydration. Geochem. Perspect. Lett. 16, 25–29. https://doi.org/10.7185/geochemlet.2039.
Connolly, J.A.D., Podladchikov, Y.Y., 2007. Decompaction weakening and channeling instability in ductile porous media: implications for asthenospheric melt segregation. J. Geophys. Res. 112 (B10), B10205. https://doi.org/10.1029/2005jb004213.
Dal Piaz, G.V., 1999. The Austroalpine-Piedmont nappe stack and the puzzle of Alpine Tethys. In: Gosso, G., et al. (Eds.), Third Meeting on Alpine Geol. Studies: Mem. Sci. Geol, 51, pp. 155–176.
Dal Piaz, G.V., 2001. History of tectonic interpretations of the Alps. J. Geodyn. 32, 99–114.

De Hoog, J.C.M., Hattori, K., Jung, H., 2014. Titanium- and water-rich metamorphic olivine in high-pressure serpentinites from the Voltri Massif (Ligurian Alps, Italy): evidence for deep subduction of high-field strength and fluid-mobile elements. Contrib. Mineral. Petrol. 167–990 https://doi.org/10.1007/s00410-014-0990-x.

de Meyer, C.M., Baumgartner, L.P., Beard, B.L., Johnson, C.M., 2014. Rb–Sr ages from phengite inclusions in garnets from high pressure rocks of the Swiss Western Alps. Earth Planet. Sci. Lett. 395, 205–216. https://doi.org/10.1016/j.epsl.2014.03.050.

Deschamps, F., Guillot, S., Godard, M., Andreani, M., Hattori, K.H., 2011. Serpentinites act as sponges for fluid-mobile elements in abyssal and subduction zone environments. Terra Nova 23, 171–178. https://doi.org/10.1111/j.1365-3121.2011.00995.x.

Deschamps, F., Godard, M., Guillot, S., Hattori, K., 2013. Geochemistry of subduction zone serpentinites: a review. Lithos 178, 96–127.

Eberhard, L., Thielmann, M., Eichheimer, P., Néri, A., Suzuki, A., Ohl, M., et al., 2022. A new method for determining fluid flux at high pressures applied to the dehydration of serpentinites. Geochem. Geophys. Geosyst. 23, e2021GC010062 https://doi.org/10.1029/2021GC010062.

Eberhard, L., Frost, D.J., McCammon, C.A., Dolejš, D., Connolly, J.A.D., 2023. Experimental constraints on the ferric Fe content and oxygen fugacity in subducted serpentinites. J. Petrol. 64, 1–18. https://doi.org/10.1093/petrology/egad069.

Eiler, J.M., Farley, K.A., Valley, J.W., Stolper, E.M., Hauri, E.H., Craig, H., 1995. Oxygen isotope evidence against bulk recycled sediment in the mantle sources of Pitcairn Island lavas. Lett. Nat. 377, 138–141.

Escher, A., Beaumont, C., 1997. Formation, burial and exhumation of basement nappes at crustal scale: a geometric model based on the Western Swiss-Italian Alps. J. Struct. Geol. 19 (7), 955–974. https://doi.org/10.1016/S0191-8141(97)00022-9.

Evans, B.W., 2004. The serpentinite multisystem revisited: chrysotile is metastable. Int. Geol. Rev. 46, 479–506. https://doi.org/10.2747/0020-6814.46.6.479.

Evans, B.W., Trommsdorff, V., 1970. Regional metamorphism of ultramafic rocks in the Central Alps: parageneses in the system CaO–MgO–SiO2–H2O. Schweiz. Mineral. Petrogr. Mitt. 50, 481–492.

Evans, B.W., Trommsdorff, V., 1978. Petrogenesis of garnet lherzolite, Cima di Gagnone, Lepontine Alps. Earth Planet. Sci. Lett. 40, 333–348.

Früh-Green, G.L., Plas, A., Lécuyer, C., 1996. 14. Petrologic and stable isotope constraints on hydrothermal alteration and serpentinization of the EPR shallow mantle at Hess Deep (Site 895). In: Proc. ODP Sci. Res, 147. Ocean Drilling Program, College Station, TX, pp. 255–293.

Früh-Green, G.L., Scambelluri, M., Vallis, F., 2001. O-H isotope ratios of high pressure ultramafic rocks: implications for fluid sources and mobility in the subducted hydrous mantle. Contrib. Mineral. Petrol. 141, 145–159. https://doi.org/10.1007/s004100000228.

Früh-Green, G.L., Connolly, J.A.D., Plas, A., Kelley, D.S., Grobety, B., 2004. Serpentinization of the oceanic peridotites: implication for geochemical cycles and biological activity. Geophys. Monogr. Ser. 144, 119–136.

Ganzhorn, A.C., Pilorgé, H., Reynard, B., 2019. Porosity of metamorphic rocks and fluid migration within subduction interfaces. Earth Planet. Sci. Lett. 522, 107–117. https://doi.org/10.1016/j.epsl.2019. 06.030.

Gilio, M., Scambelluri, M., Agostini, S., Godard, M., Peters, D., Pettke, T., 2019. Petrology and geochemistry of serpentinites associated with the ultra-high pressure Lago di Cignana Unit (Italian Western Alps). J. Petrol. 60 (6), 1229–1262. https://doi.org/10.1093/petrology/egz030.

Gregory, R.T., Taylor, H.P., 1981. An oxygen isotope profile in a section of cretaceous oceanic crust, Samail Ophiolite, Oman: evidence for δ18O buffering of the oceans by deep (>5km) seawater-hydrothermal circulation at mid-oceanic ridges. J. Geophys. Res. 86, 2737–2755.

Hacker, B.R., Peacock, S.M., Abers, G.A., Holloway, S.D., 2003. Subduction factory 2. Are intermediate-depth earthquakes in subducting slabs linked to metamorphic dehydration reactions? J. Geophys. Res. 108 (B1), 2030. https://doi.org/10.1029/2001JB001129.

Hellebrand, E., Snow, J.E., Dick, H.J., Hofmann, A.W., 2001. Coupled major and trace elements as indicators of the extent of melting in mid-ocean- ridge peridotites. Nature 410 (6829), 677. https://doi.org/10.1038/35070546.

Hellebrand, E., Snow, J.E., Mühe, R., 2002. Mantle melting beneath Gakkel Ridge (Arctic Ocean): abyssal peridotite spinel compositions. Chem. Geol. 182 (2–4), 227–235. https://doi.org/10.1016/S0009-2541(01)00291-1.

Hellstrom, J., Paton, C., Woodhead, J., Hergt, J., 2008. Laser ablation ICP–MS in the earth sciences: Current practices and outstanding issues. In: Sylvester, P. (Ed.), Laser Ablation ICP–MS in the Earth Sciences: Current Practices and Outstanding Issues, 40, pp. 343–348.

Herms, P., John, T., Bakker, R.J., Schenk, V., 2012. Evidence for channelized external fluid flow and element transfer in subducting slabs (Raspas Complex, Ecuador). Chem. Geol. 310–311, 79–96. https://doi.org/10.1016/j.chemgeo.2012.03.023.

Holland, T., Powell, R., 1998. An internally consistent thermodynamic data set for phases of petrological interest. J. Metamorph. Geol. 16 (3), 309–343. https://doi.org/10.1111/j.1525-1314.1998.00140.x.

Holland, T., Baker, J., Powell, R., 1998. Mixing properties and activity-composition relationships of chlorites in the system MgO-FeO-Al2O3-SiO2-H2O. Eur. J. Mineral. https://doi.org/10.1127/ejm/10/3/0395.

Huang, F., Sverjensky, D.A., 2019. Extended deep earth water model for predicting major element mantle metasomatism. Geochim. Cosmochim. Acta 254, 192–230. https://doi.org/10.1016/j.gca.2019.03.027.

Huber, K., Vrijmoed, J.C., John, T., 2022. Formation of olivine veins by reactive fluid flow in a dehydrating serpentinite. Geochem. Geophys. Geosyst. 23, e2021GC010267 https://doi.org/10.1029/2021GC010267.

Huberty, J.M., Kita, N.T., Kozdon, R., Heck, P.R., Fournelle, J.H., Spicuzza, M.J., Xu, H., Valley, J.W., 2010. Crystal orientation effects in δ18O for magnetite and hematite by SIMS. Chem. Geol. 276 (3–4), 269–283. https://doi.org/10.1016/j.chemgeo.2010.06.012.

Isa, J., Kohl, I.E., Liu, M.-C., Wasson, J.T., Young, E.D., McKeegan, K.D., 2017. Quantification of oxygen isotope SIMS matrix effects in olivine samples: correlation with sputter rate. Chem. Geol. 458, 14–21. https://doi.org/10.1016/j.chemgeo.2017.03.020.

Jabaloy-Sánchez, A., Sánchez-Vizcaíno, V.L., Padrón-Navarta, J.A., Hidas, K., Gómez-Pugnaire, M.T., Garrido, C.J., 2022. Olivine-rich veins in high-pressure serpentinites: a far-field paleo-stress snapshot during subduction. J. Struct. Geol. 163, 104721 https://doi.org/10.1016/j.jsg.2022.104721.

Jochum, K.P., Nohl, U., Herwig, K., Lammel, E., Stoll, B., Hofmann, A.W., 2007. GeoReM: a new geochemical database for reference materials and isotopic standards. Geostand. Geoanal. Res. 29 (3), 333–338. https://doi.org/10.1111/j.1751-908X.2005.tb00904.x.

Jones, C.E., Jenkyns, H.C., Hesselbo, S.P., 1994. Strontium isotopes in Early Jurassic seawater. Geochim. Cosmochim. Acta 58 (4), 1285–1301. https://doi.org/10.1016/0016-7037(94)90382-4.

Kawano, S., Katayama, I., Okazaki, K., 2011. Permeability anisotropy of serpentinite and fluid pathways in a subduction zone. Geology 39, 939–942. https://doi.org/10.1130/G32173.1.

Kempf, E.D., Reusser, E., Baumgartner, L.P., Connolly, J.A.D., 2014. Reactive Transport in Serpentinites (Zermatt, Switzerland). unpublished Master Thesis. ETH Zürich.

Kempf, E.D., Hermann, J., Reusser, E., Baumgartner, L.P., Lanari, P., 2020. The role of the antigorite + brucite to olivine reaction in subducted serpentinites (Zermatt, Switzerland). Swiss J. Geosci. 113, 16. https://doi.org/10.1186/s00015-020-00368-0.

Kita, N.T., Huberty, J.M., Kozdon, R., Beard, B.L., Valley, J.W., 2010. High-precision SIMS oxygen, sulfur and iron stable isotope analyses of geological materials: accuracy, surface topography and crystal orientation. Surf. Interface Anal. 43 https://doi.org/10.1002/sia.3424.

Kodolányi, J., Pettke, T., Spandler, C., Kamber, B.S., Gméling, K., 2012. Geochemistry of ocean floor and fore-arc serpentinites: constraints on the ultrabasic input to subduction zones. J. Petrol. 53, 235–270. https://doi.org/10.1093/petrology/egr058.

Kozdon, R.K., Kita, N.T., Huberty, J.M., Fournelle, J.H., Valley, J.W., 2010. In situ sulfur isotope analysis of sulfide minerals by SIMS: precision and accuracy, with application to thermometry of 3.5 Ga Pilbara cherts. Chem. Geol. 275 (3–4), 243–253.

Lafay, R., Deschamps, F., Schwartz, S., Guillot, S., Godard, M., Debret, B., Nicollet, C., 2013. High-pressure serpentinites, a trap-and-release system controlled by metamorphic conditions: example from the Piedmont zone of the western Alps. Chem. Geol. 343, 38–54. https://doi.org/10.1016/j.chemgeo.2013.02.008.

Lakey, S., Hermann, J., 2022. An experimental study of chlorite stability in varied subduction zone lithologies with implications for fluid production, melding, and diapirism in chlorite-rich Mélange rocks. J. Petrol. 63 (4), 1–29. https://doi.org/10.1093/petrology/egac029.

Lanari, P., Duesterhoeft, E., 2019. Modeling metamorphic rocks using equilibrium thermodynamics and internally consistent databases: past achievements, problems and perspectives. J. Petrol. 60, 19–56. https://doi.org/10.1093/petrology/egy105.

Lanari, P., Engi, M., 2017. Local bulk composition effects on metamorphic mineral assemblages. Rev. Mineral. Geochem. 83 (1), 55–102. https://doi.org/10.2138/rmg.2017.83.3.

Lanari, P., Vidal, O., De Andrade, V., Dubacq, B., Lewin, E., Grosch, E.G., et al., 2014. XMapTools: a MATLAB©-based program for electron micro- probe X-ray image processing and geothermobarometry. Comput. Geosci. 62, 227–240. https://doi.org/10.1016/j.cageo.2013.08.010.

Lanari, P., Vho, A., Bovay, T., Airaghi, L., Centrella, S., 2019. Quantitative compositional mapping of mineral phases by electron probe micro-analyser. Geol. Soc. Lond. Spec. Publ. 478 (1), 39–63. https://doi.org/10.1144/SP478.4.

Lapen, T.J., Johnson, C.M., Baumgartner, L.P., Mahlen, N.J., Beard, B.L., Amato, J.M., 2003. Burial rates during prograde metamorphism of an ultra-high-pressure terrane: an example from Lago di Cignana, western Alps, Italy. Earth Planet. Sci. Lett. 215 (1–2), 57–72. https://doi.org/10.1016/S0012-821X(03)00455-2.

Li, X.P., Rahn, M., Bucher, K., 2004. Serpentinites of the Zermatt-Saas ophiolite complex and their texture evolution. J. Metamorph. Geol. 22 (3), 159–177. https://doi.org/10.1111/j.1525-1314.2004.00503.x.

Li, X.P., Rahn, M., Bucher, K., 2008. Eclogite facies metarodingites-phase relations in the system SiO2-Al2O3-Fe2O3-FeO-MgO-CaO-CO2-H2O: an example from the Zermatt-Saas ophiolite. J. Metamorph. Geol. 26 (3), 347–364. https://doi.org/10.1111/j.1525-1314.2008.00761.x.

Lyon, I.C., Saxton, J.M., Cornah, S.J., 1998. Isotopic fractionation during secondary ionisation mass spectrometry: crystallographic orientation effects in magnetite. Int. J. Mass Spectrom. Ion Process. 172 (1–2), 115–122.

Marin-Carbonne, J., Rollion-Bard, C., Luais, B., 2011. In-situ measurements of iron isotopes by SIMS: MC-ICP-MS intercalibration and application to a magnetite crystal from the Gunflint chert. Chem. Geol. 285, 50–61. https://doi.org/10.1016/j.chemgeo.2011.02.019.

Mattey, D., Lowry, D., Macpherson, C., 1994. Oxygen isotope composition of mantle peridotite. Earth Planet. Sci. Lett. 128 (3–4), 231–241. https://doi.org/10.1016/0012-821X(94)90147-3.

McDonough, W.F., Sun, S.-S., 1995. The composition of the Earth. Chem. Geol. 120, 223–253. https://doi.org/10.1016/0009-2541(94)00140-4.

Miller, S.A., van der Zee, W., Olgaard, D.L., Connolly, J.A.D., 2003. A fluid-pressure feedback model of dehydration reactions: experiments, modelling, and application to subduction zones. Tectonophysics 370 (1), 241–251. https://doi.org/10.1016/S0040-1951(03)00189-6.

Padrón-Navarta, J.A., López Sánchez-Vizcaíno, V., Garrido, C.J., Gómez-Pugnaire, M.T., Jabaloy, A., Capitani, G., Mellini, M., 2008. Highly ordered antigorite from Cerro del Almirez HP–HT serpentinites, SE Spain. Contrib. Mineral. Petrol. 156, 679–688.
Padrón-Navarta, J.A., Tommasi, A., Garrido, C.J., Sánchez-Vizcaíno, V.L., Gómez-Pugnaire, M.T., Jabaloy, A., Vauchez, A., 2010. Fluid transfer into the wedge controlled by high-pressure hydrofracturing in the cold top-slab mantle. Earth Planet. Sci. Lett. 297 (1), 271–286. https://doi.org/10.1016/j.epsl.2010.06.029.
Padrón-Navarta, J.A., Lopez Sanchez-Vizcaino, V., Garrido, C.J., Gómez-Pugnaire, M.T., 2011. Metamorphic record of high-pressure dehydration of antigorite serpentinite to chlorite harzburgite in a subduction setting (Cerro del Almirez, Nevado–Filábride Complex, Southern Spain). J. Petrol. 52, 2047–2078.
Padrón-Navarta, J.A., Sánchez-Vizcaíno, V.L., Hermann, J., Connolly, J.A.D., Garrido, C. J., Gómez-Pugnaire, M.T., Marchesi, C., 2013. Tschermak's substitution in antigorite and consequences for phase relations and water liberation in high-grade serpentinites. Lithos 178, 186–196. https://doi.org/10.1016/j.lithos.2013.02.001.
Pagé, L., Hattori, K., 2017. Tracing halogen and B cycling in subduction zones based on obducted, subducted and forearc serpentinites of the Dominican Republic. Sci. Rep. 7, 17776. https://doi.org/10.1038/s41598-017-18139-7.
Paton, C., Hellstrom, J., Paul, B., Woodhead, J., Hergt, J., 2011. Iolite: freeware for the visualisation and processing of mass spectrometric data. J. Anal. At. Spectrom. 26, 2508–2518.
Peterman, Z.E., Hedge, C.E., Tourtelot, H.A., 1970. Isotopic composition of strontium in sea water throughout Phanerozoic time. Geochim. Cosmochim. Acta 34 (1), 105–120. https://doi.org/10.1016/0016-7037(70)90154-7.
Peters, D., Pettke, T., 2017. Evaluation of major to ultra trace element bulk rock chemical analysis of nanoparticulate pressed powder pellets by LA-ICP-MS. Geostand. Geoanal. Res. 41, 5–28. https://doi.org/10.1111/ggr.12125.
Peters, D., Bretscher, A., John, T., Scambelluri, M., Pettke, T., 2017. Fluid-mobile elements in serpentinites: constraints on serpentinisation environments and element cycling in subduction zones. Chem. Geol. 466, 654–666. https://doi.org/10.1016/j.chemgeo.2017.07.017.
Peters, D., Pettke, T., John, T., Scambelluri, M., 2020. The role of brucite in water and element cycling during serpentinite subduction – Insights from Erro Tobbio (Liguria, Italy). Lithos 360–361, 105431. https://doi.org/10.1016/j.lithos.2020.105431.
Pettke, T., Bretscher, A., 2022. Fluid-mediated element cycling in subducted oceanic lithosphere: the orogenic serpentinite perspective. Earth Sci. Rev. 225, 103896 https://doi.org/10.1016/j.earscirev.2021.103896.
Plas, A., 1997. Petrologic and stable isotope constraints on fluid-rock interaction, serpentinization and alteration of oceanic ultramafic rocks. Ph.D thesis, No. 12261. ETH-Zürich, 252 pp.
Plümper, O., John, T., Podladchikov, Y.Y., Vrijmoed, J.C., Scambelluri, M., 2017. Fluid escape from subduction zones controlled by channel-forming reactive porosity. Nat. Geosci. 10 (2), 150–156. https://doi.org/10.1038/ngeo2865.
Rouméjon, S., Williams, M.J., Früh-Green, G.L., 2018. In-situ oxygen isotope analyses in serpentine minerals: constraints on serpentinization during tectonic exhumation at slow- and ultraslow-spreading ridges. Lithos 323, 156–173. https://doi.org/10.1016/j.lithos.2018.09.021.
Rubatto, D., Angiboust, S., 2015. Oxygen isotope record of oceanic and high-pressure metasomatism: a P-T-time-fluid path for the Monviso eclogites (Italy). Contrib. Mineral. Petrol. 170 (44) https://doi.org/10.1007/s00410-015-1198-4.
Rubatto, D., Gebauer, D., Fanning, M., 1998. Jurassic formation and Eocene subduction of the Zermatt–Saas-Fee ophiolites: implications for the geodynamic evolution of the Central and Western Alps. Contrib. Mineral. Petrol. 132 (3), 269–287. https://doi.org/10.1007/s004100050421.
Rubatto, D., Williams, M., Markmann, T.A., Hermann, J., Lanari, P., 2023. Tracing fluid infiltration into oceanic crust up to ultra-high-pressure conditions. Contrib. Mineral. Petrol. 178 (79) https://doi.org/10.1007/s00410-023-02060-6.
Rüpke, L., Morgan, J.P., Hort, M., Connolly, J.A.D., 2004. Serpentine and the subduction zone water cycle. Earth Planet. Sci. Lett. 223 (1), 17–34. https://doi.org/10.1016/j.epsl.2004.04.018.
Saccocia, P.J., Seewald, J.S., Shanks, W.C., 2009. Oxygen and hydrogen isotope fractionation in serpentine–water and talc–water systems from 250 to 450°C, 50 MPa. Geochim. Cosmochim. Acta 73, 6789–6804.
Savov, I.P., Guggino, S., Ryan, J.G., Fryer, P., Mottl, M.J., 2005. Geochemistry of serpentinite muds and metamorphic rocks from the Mariana Forearc, ODP Sites 1200 and 778–779, South Chamorro and Conical Seamounts. Proc. Ocean Drill. Program Sci. Results 195, 1–49.
Savov, I.P., Ryan, J.G., D'Antonio, M., Fryer, P., 2007. Shallow slab fluid release across and along the Mariana arc-basin system: insights from geochemistry of serpentinized peridotites from the Mariana fore arc. J. Geophys. Res. 112 (B9), 1–30. https://doi.org/10.1029/2006JB004749.
Scambelluri, M., Tonarini, S., 2012. Boron isotope evidence for shallow fluid transfer across subduction zones by serpentinized mantle. Geology 40 (10), 907–910. https://doi.org/10.1130/G33233.1.
Scambelluri, M., Müntener, O., Hermann, J., Piccardo, G.B., Trommsdorff, V., 1995. Subduction of water into the mantle: history of an Alpine peridotite. Geology 23 (5), 459–462.
Scambelluri, M., Müntener, O., Ottolini, L., Pettke, T., Vannucci, R., 2004a. The fate of B, Cl and Li in the subducted oceanic mantle and in the antigorite-breakdown fluids. Earth Planet. Sci. Lett. 222, 217–234. https://doi.org/10.1016/j.epsl.2004.02.012.
Scambelluri, M., Fiebig, J., Malaspina, N., Müntener, O., Pettke, T., 2004b. Serpentinite subduction: implications for fluid processes and trace-element recycling. Int. Geol. Rev. 46 (7), 595–613. https://doi.org/10.2747/0020-6814.46.7.595.
Scambelluri, M., Cannaò, E., Gilio, M., 2019. The water and fluid-mobile element cycles during serpentinite subduction. A review. Eur. J. Mineral. 31, 405–428. https://doi.org/10.1127/ejm/2019/0031-2842.
Schmidt, M.W., Poli, S., 1998. Experimentally based water budgets for dehydrating slabs and consequences for arc magma generation. Earth Planet. Sci. Lett. 163 (1), 361–379. https://doi.org/10.1016/S0012-821X(98)00142-3.
Schwartz, S., Guillot, S., Reynard, B., Lafay, R., Debret, B., Nicollet, C., Lanari, P., Auzende, A.L., 2013. Pressure-temperature estimates of the lizardite/antigorite transition in high pressure serpentinites. Lithos 178, 197–210. https://doi.org/10.1016/j.lithos.2012.11.023.
Scicchitano, M.R., Rubatto, D., Hermann, J., Shen, T., Padrón-Navarta, J.A., Williams, I. S., Zheng, Y.-F., 2018. In situ oxygen isotope determination in serpentine minerals by ion microprobe: reference materials and applications to ultrahigh-pressure serpentinites. Geostand. Geoanal. Res. 42 (4), 459–479. https://doi.org/10.1111/ggr.12232.
Scicchitano, M.R., Rubatto, D., Hermann, J., Majumdar, A.S., Putnis, A., 2018b. Oxygen isotope analysis of olivine by ion microprobe: matrix effects and applications to a serpentinised dunite. Chem. Geol. 499, 126–137. https://doi.org/10.1016/j.chemgeo.2018.09.020.
Scicchitano, M.R., Spicuzza, M.J., Ellison, E.T., Tuschel, D., Templeton, A.S., Valley, J. W., 2020. *In situ* oxygen isotope determination in serpentine minerals by SIMS: addressing matrix effects and providing new insights on serpentinisation at hole BA1B (Samail ophiolite, Oman). Geostand. Geoanal. Res. 45 (1), 161–187. https://doi.org/10.1111/ggr.12359.
Scicchitano, M.R., Lafay, R., Valley, J.W., Kita, N.T., Nachlas, W.O., 2022. Protracted hydrothermal alteration recorded at the microscale in the Chenaillet ophicarbonates (Western Alps): insights from *in situ* $\delta^{18}O$ thermometry in serpentine, carbonate and magnetite. Geochim. Cosmochim. Acta 318, 144–164. https://doi.org/10.1016/j.gca.2021.11.025.
Seydoux, L., Baumgartner, L.P., 2013. Interactions fluide-roche dans les ultramafiques de la zone de Zermatt-Saas Fee. unpublished Master Thesis. University of Lausanne.
Seyfried, W.E., Dibble, W.E., 1980. Seawater-peridotite interaction at 300°C and 500 bars: implications for the origin of oceanic serpentinites. Geochim. Cosmochim. Acta 44, 309–321. https://doi.org/10.1016/0016-7037(80)90139-8.
Skarbek, R.M., Rempel, A.W., 2016. Dehydration-induced porosity waves and episodic tremor and slip. Geochem. Geophys. Geosyst. 17 (2), 442–469. https://doi.org/10.1002/2015GC006155.
Skora, S., Mahlen, N., Johnson, C.M., Baumgartner, L.P., Lapen, T., Beard, B.L., et al., 2015. Evidence for protracted prograde metamorphism followed by rapid exhumation of the Zermatt-Saas Fee ophiolite. J. Metamorph. Geol. 33 (7), 711–734. https://doi.org/10.1111/jmg.12148.
Spandler, C., Pettke, T., Rubatto, D., 2011. Internal and external fluid sources for eclogite-facies veins in the Monviso meta-ophiolite, Western Alps: implications for fluid flow in subduction zones. J. Petrol. 52 (6), 1207–1236. https://doi.org/10.1093/petrology/egr025.
Tenthorey, E., Hermann, J., 2004. Composition of fluids during serpentinite break-down in subduction zones: evidence for limited boron mobility. Geology 32 (10), 865–868. https://doi.org/10.1130/G20610.1.
Thompson, G., Melson, W.G., 1970. Boron contents of serpentinites and metabasalts in the oceanic crust: implications for the boron cycle in the oceans. Earth Planet. Sci. Lett. 8 (1), 61–65. https://doi.org/10.1016/0012-821X(70)90100-7.
Tiraboschi, C., Tumiati, S., Sverjensky, D.A., Pettke, T., Ulmer, P., Poli, S., 2017. Experimental determination of magnesia and silica solubilities in graphite-saturated and redox-buffered high-pressure COH fluids in equilibrium with forsterite + enstatite and magnesite + enstatite. Contrib. Mineral. Petrol. 173, 2. https://doi.org/10.1007/s00410-017-1427-0.
Tollan, P.M.E., Bindeman, I., Blundy, J.D., 2012. Cumulate xenoliths from St. Vincent, Lesser Antilles Island Arc: a window into upper crustal differentiation of mantle-derived basalts. Contrib. Mineral. Petrol. 163, 189–208. https://doi.org/10.1007/s00410-011-0665-9.
Trommsdorff, V., Sánchez-Vizcaíno, V.L., Gomez-Pugnaire, M., Müntener, O., 1998. High pressure breakdown of antigorite to spinifex-textured olivine and orthopyroxene, SE Spain. Contrib. Mineral. Petrol. 132, 139–148.
Trommsdorff, V., Hermann, J., Müntener, O., Pfiffner, M., Risold, A.-C., 2000. Geodynamic cycles of subcontinental lithosphere in the Central Alps and the Arami enigma. J. Geodyn. 30, 77–92.
Ulmer, P., Trommsdorff, V., 1995. Serpentine stability to mantle depths and subduction-related magmatism. Science 268 (5212), 858–861. https://doi.org/10.1126/science.268.5212.858.
Vesin, C., Rubatto, D., Pettke, T., Deloule, E., 2023. Multistage hydration during oceanic serpentinisation revealed by in situ oxygen isotope and trace element analyses. Geochim. Cosmochim. Acta 355, 13–31. https://doi.org/10.1016/j.gca.2023.06.032.
Vho, A., Rubatto, D., Lanari, P., 2019. An internally-consistent database for oxygen isotope fractionation between minerals. J. Petrol. 60 (11), 2101–2130. https://doi.org/10.1093/petrology/egaa001.
Vho, A., Lanari, P., Rubatto, D., Hermann, J., 2020. Tracing fluid transfers in subduction zones: an integrated thermodynamic and δ18O fractionation modelling approach. Solid Earth 11, 307–328. https://doi.org/10.5194/se-11-307-2020.
Vieira Duarte, J.F., Piccoli, F., Pettke, T., Hermann, J., 2021. Textural and geochemical evidence or magnetite production upon antigorite breakdown during subduction. J. Petrol. 62 (10), 1–29. https://doi.org/10.1093/petrology/egab053.
Vils, F., Pelletier, L., Kalt, A., Müntener, O., Ludwig, T., 2008. The lithium, boron and beryllium content of serpentinized peridotites from ODP Leg 209 (Sites 1272A and 1274A): implications for lithium and boron budgets of oceanic lithosphere. Geochim. Cosmochim. Acta 72, 5475–5504.
Wenner, D.B., Taylor, H.P., 1971. Temperatures of serpentinization of ultramafic rocks based on O^{18}/O^{16} fractionation between coexisting serpentine and magnetite. Contrib. Mineral. Petrol. 32, 165–185. https://doi.org/10.1007/BF00643332.

White, L., Vasconcelos, P.M., Ávila, J.N., Ubide, T., Ireland, T.R., 2021. Crystallographic and crystallochemical controls on oxygen isotope analysis of hematite by SIMS. Chem. Geol. 583, 120461 https://doi.org/10.1016/j.chemgeo.2021.120461.
Whitney, D.L., Evans, B.W., 2010. Abbreviations for names of rock-forming minerals. Am. Mineral. 95, 185–187. https://doi.org/10.2138/am.2010.3371.
Widmer, T.W., 1996. Entwässerung ozeanisch alterierter Basalte in Subduktionszonen (Zone von Zermatt-Saas Fee). Ph.D. thesis, No. 11609. ETH-Zürich, 219 pp.
Zheng, Y.-F., 1993a. Calculation of oxygen isotope fractionation in anhydrous silicate minerals. Geochim. Cosmochim. Acta 57, 3199–1091.
Zheng, Y.-F., 1993b. Calculation of oxygen isotope fractionation in hydroxyl-bearing silicates. Earth Planet. Sci. Lett. 120, 247–263.